

Technical Report 1244

Design and Control of a Closed-Loop Brushless Torque Activator

Michael Dean Levin

MIT Artificial Intelligence Laboratory

REPORT DOCUMENTATION PAGE			Form Approved OMB No. 0704-0188	
Public reporting burden for this collection of information is estimated to average 1 hour per response, including the time for reviewing instructions, searching existing data sources, gathering and maintaining the data needed, and completing and reviewing the collection of information. Send comments regarding this burden estimate or any other aspect of this collection of information, including suggestions for reducing this burden, to Washington Headquarters Services, Directorate for Information Operations and Reports, 1215 Jefferson Davis Highway, Suite 1204, Arlington, VA 22202-4302, and to the Office of Management and Budget, Paperwork Reduction Project (0704-0188), Washington, DC 20503.				
1. AGENCY USE ONLY (Leave blank)	2. REPORT DATE May 1990	3. REPORT TYPE AND DATES COVERED technical report		
4. TITLE AND SUBTITLE Design and Control of a Closed-Loop Brushless Torque Actuator		5. FUNDING NUMBERS N00014-86-K-0685		
6. AUTHOR(S) Michael Dean Levin				
7. PERFORMING ORGANIZATION NAME(S) AND ADDRESS(ES) Artificial Intelligence Laboratory 545 Technology Square Cambridge, Massachusetts 02139		8. PERFORMING ORGANIZATION REPORT NUMBER AI-TR 1244		
9. SPONSORING / MONITORING AGENCY NAME(S) AND ADDRESS(ES) Office of Naval Research Information Systems Arlington, Virginia 22217		10. SPONSORING / MONITORING AGENCY REPORT NUMBER AD-A270760		
11. SUPPLEMENTARY NOTES None				
12a. DISTRIBUTION / AVAILABILITY STATEMENT Distribution of this document is unlimited		12b. DISTRIBUTION CODE		
13. ABSTRACT (Maximum 200 words) This report explores the design and control issues associated with a brushless actuator capable of achieving extremely high torque accuracy. Models of several different motor - sensor configurations were studied to determine dynamic characteristics. A reaction torque sensor fixed to the motor stator was implemented to decouple the transmission dynamics from the sensor. This resulted in a compact actuator with higher bandwidth and precision than could be obtained with an inline or joint sensor. Quasi-static testing demonstrated a closed-loop torque accuracy within 0.1% over the full range of torques. Torque ripple and friction effects, which accounted for errors of up to 7% in open-loop tests, were virtually eliminated. The mechanical bandwidth of the system approaches 300 Hz, but the current loop in the drive electronics limits the open-loop bandwidth to less than 10 Hz. Compensation techniques were utilized to increase the controllable bandwidth to greater than 200 Hz, demonstrating that the motor response can be drastically improved by closing a high bandwidth torque loop.				
14. SUBJECT TERMS (key words) torque control reaction torque brushless motors			15. NUMBER OF PAGES 110	
			16. PRICE CODE \$8.00	
17. SECURITY CLASSIFICATION OF REPORT UNCLASSIFIED	18. SECURITY CLASSIFICATION OF THIS PAGE UNCLASSIFIED	19. SECURITY CLASSIFICATION OF ABSTRACT UNCLASSIFIED	20. LIMITATION OF ABSTRACT UNCLASSIFIED	

Design and Control of a Closed-Loop Brushless Torque Actuator

by

Michael Dean Levin

S.B. (1987) Aeronautical & Astronautical Engineering
Massachusetts Institute of Technology

**Submitted to the Department of
Mechanical Engineering
in Partial Fulfillment of the Requirements
for the Degree of**

**Master of Science
in Mechanical Engineering**

at the

Massachusetts Institute of Technology

May, 1990

©Massachusetts Institute of Technology 1990
All rights reserved

Design and Control of a Closed-Loop Brushless Torque Actuator

by

Michael D. Levin

*Submitted to the Department of Mechanical Engineering on May 11, 1990
in partial fulfillment of the requirements for the Degree of Master of Science
in Mechanical Engineering*

Abstract

This report explores the design and control issues associated with a brushless actuator capable of achieving extremely high torque accuracy. Models of several different motor - sensor configurations were studied to determine dynamic characteristics. A reaction torque sensor fixed to the motor stator was implemented to decouple the transmission dynamics from the sensor. This resulted in a compact actuator with higher bandwidth and precision than could be obtained with an inline or joint sensor.

Quasi-static testing demonstrated a closed-loop torque accuracy within 0.1% over the full range of torques. Torque ripple and friction effects, which accounted for errors of up to 7% in open-loop tests, were virtually eliminated. The mechanical bandwidth of the system approaches 300 Hz, but the current loop in the drive electronics limits the open-loop bandwidth to less than 10 Hz. Compensation techniques were utilized to increase the controllable bandwidth to greater than 200 Hz, demonstrating that the motor response can be drastically improved by closing a high bandwidth torque loop.

Thesis Supervisor:

Dr. J. Kenneth Salisbury, Jr.
Research Scientist
MIT Artificial Intelligence Laboratory

Acknowledgments

This thesis describes research conducted at the Artificial Intelligence Laboratory of the Massachusetts Institute of Technology. Support for the laboratory's artificial intelligence research is provided in part by the Office of Naval Research University Initiative Program under the Office of Naval Research contract N00014-86-K-0685.

My advisor, Ken Salisbury, provided invaluable guidance and suggestions. His motivation and insight kept me going when I encountered unforeseen obstacles or had doubts. Ken's knowledge, imagination, and dedication have made him a leader in his field, and an honor and pleasure to work with.

Brian Eberman assisted with a significant portion of the analysis and design of the actuator. He and Gunter Niemeyer developed the operating system and provided countless control improvements and software fixes. Tom Moyer and Peter Graham supplied needed diversions, food, and cycling and didn't let me lose perspective. Late night discussions with Dave Brock and Camille Chammas increased my understanding of other research in the field of robotics. Bill Townsend designed and built the original *Whole Arm Manipulator*.

Erik Vaaler checked and improved many aspects of the actuator design. Ron Wiken aided in the electrical assembly. Randy, Mike, and Mike at RAMCO delivered perfect parts in near record time.

Tim Hawkey and Dave Stracher didn't let me bring the stress of work home with me. Dart games with them and Lee Hetherington were a guaranteed way to relax. Lee also allowed me to use his Macintosh at all hours of the day and night when the mechanical parts had to be redesigned.

My parents, Simon and Judith, gave me the opportunity to pursue my goals, with a never-ending supply of love and encouragement along the way. My brother Dan and sister Elise made sure I was always politically correct and having fun, respectively.

Finally, my fiancée, Heidi Eigenrauch, has been a constant source of love, support, and companionship. She came up with the most appropriate title for this thesis: "Mikey's Magical Motor & It's Many Magnificent Motions." Heidi's smile and laughter helped me through the rough times, and the weeks without seeing her motivated me to finish early. Our future looks bright. Thanks for everything H, ily.

Contents

1	Introduction	8
1.1	Robotic Capabilities and Control	8
1.1.1	Force Control	9
1.1.2	Whole-Arm Manipulation	13
1.2	Thesis Overview	15
2	Torque Control Design Considerations	17
2.1	Bandwidth and Dynamic Range	18
2.1.1	Whole Arm Manipulator Design	19
2.1.2	Actuator Design Goals	21
2.2	Design Options	22
2.2.1	Motor Selection	22
2.2.2	Sensor Criteria	27
3	Design	35
3.1	Hardware Design	35
3.1.1	Actuator	35
3.1.2	Drive Electronics	39
3.2	Development System	42
3.2.1	Condor Hardware	42
3.2.2	Condor Software Support	43
3.3	Software Implementation	45
4	System Model	48
4.1	Motor Model	48
4.2	Sensor Model	53
4.3	Controller Model	53

4.4	Bandwidth Estimation	56
4.5	Torque Ripple	58
4.6	Friction Models	62
5	Results	65
5.1	Open Loop Actuator Characteristics	65
5.1.1	Bearing Friction	65
5.1.2	Sensor Calibration	66
5.1.3	Torque Ripple	67
5.2	Open vs Closed-Loop Performance	68
5.3	Dynamic Response	72
6	Conclusion	80
6.1	Summary	80
6.2	Problem Areas	82
6.3	Future Research	83
A	Actuator Drawings	85
B	Component Specifications	98

List of Figures

1.1	The MIT Whole-Arm Manipulator.	15
2.1	A Two Stage Cable Transmission.	19
2.2	Conventional DC Motor Layout.	22
2.3	Brushless DC Motor Layout.	23
2.4	Comparision of Trapezoidal and Sine Wave Commutation.	26
2.5	Reaction Torque Sensor - Lumped Parameter Model.	28
2.6	Inline Torque Sensor - Lumped Parameter Model.	30
2.7	Joint Torque Sensor - Lumped Parameter Model.	32
3.1	Actuator layout.	37
3.2	Functional Layout of a Brushless Motor Controller.	41
3.3	MIT-WAM Control Hardware Block Diagram.	44
4.1	Stator Equivalent Circuit.	48
4.2	Theoretical Torque - Speed Curve.	51
4.3	High Level Control Block Diagram.	54
4.4	First Harmonic for a Three Pole Pair Brushless Motor.	60
4.5	Second Harmonic for a Three Pole Pair Brushless Motor.	62
4.6	Common Models of Friction.	63
5.1	Clockwise and Counter Clockwise Torque with Motor Disabled.	66
5.2	Effect of Ripple on CW and CCW Rotation.	67
5.3	Open Loop Torque and 2nd Ripple Harmonic.	68
5.4	Open and Closed Loop Torque at 0 in-lb Command.	69
5.5	Open Loop Torque in Both Directions at 0.5 in-lb Command.	70
5.6	Open and Closed Loop Torque at 5.0 in-lb Command.	71
5.7	Magnification of Closed Loop Torque at 5.0 in-lb Command.	72

5.8	Frequency Response of the Open Loop System.	73
5.9	Response of the Open Loop System at Low Frequencies.	75
5.10	Low Frequency Response with Small Amplitude Excitation. . . .	76
5.11	Step Response of the Open Loop System.	77
5.12	Step Response with PID Compensation.	78

Chapter 1

Introduction

1.1 Robotic Capabilities and Control

There are many definitions for robots in society today. Some consider numerically controlled machines as robots, where others restrict their view to devices that assemble or paint along an assembly line. Children envision androids like C3PO, or versatile machines that can do anything such as Rosie, the automated maid on the Jetsons. Isaac Asimov gave them a life-like appearance and personality, and even the ability to read minds.

Unfortunately, the state of the art in robotics is not quite that advanced. Most robots can only follow preprogrammed commands, and are typically used for assembly, painting, or materials handling. Those more advanced can make remedial decisions based upon some sensor inputs. Research is taking place to enable machines to ‘learn’ through neural networks. The Mobile Robotics group in the MIT Artificial Intelligence lab has built several mechanical creatures with embedded behaviors. These devices can respond to various stimuli: light, sound, movement. By layering these different behaviors, the robots are given a limited personality. Truly human reasoning, however, is still a long

way off.

In the near future, robotics will play a major role in building and maintaining the space station. They will be required to be agile and quick, capable of moving massive loads, yet delicate enough to fasten connectors. Unstructured environments such as space or undersea present a great challenge to the field of robotics, since programmed behaviors can be inadequate as the situation changes. Long communication delays prohibit purely teleoperated mechanisms. Future manipulators will need to be autonomous, and prepared for a variety of unexpected occurrences. They will also be required to be versatile, as NASA would prefer to send up one general purpose device rather than several machines, each capable of performing only a single function.

1.1.1 Force Control

In virtually all robotic applications, it is necessary to interact with the environment to achieve a task. Many of these tasks require precise control of forces to effectively manipulate an object without damage to it or the robotic device. It is desirable to control contact forces while executing assembly or pick and place tasks, as well as being able to monitor any collisions. As tasks become more complex and environments less structured, there will be an even greater need for accurate, high bandwidth force control. One of the major thrusts of current robotics research is therefore in the area of force control.

An overview of the history of force control was presented by Whitney [Whitney 85]. He reviewed the major strategies involved in force control and analyzed stability. Maples [Maples 86] described and categorized some of these methods.

Force control techniques can be categorized as passive, active, or a combination of the two. Passive methods are best represented by Remote Center Compliance (RCC) devices. This device was developed by Drake [Drake 77] at Draper labs and uses compliance to control and limit forces at the end-effector.

In active force control, manipulator forces are controlled through actuator commands. In some cases, feedforward control is sufficient to achieve the desired force accuracy. In this method, the joint torques are adjusted through servo gains to achieve the desired manipulator stiffness. This implicit force control is suitable when the manipulator dynamics are known, and the environment is predetermined and relatively static. An [An 86] used a type of implicit control on the MIT Serial Link Direct Drive Arm to control the interaction force at the end-effector.

Paul [Paul 72] precomputed the required torques using Lagrangian equations. This computed torque was then the command torque at the joint. As the manipulator moved, its dynamics changed, requiring computation of a new torque command. This approach used large amounts of processing time due to the complexity of accurate dynamic equations.

The addition of force sensors enables higher precision feedback control. There are four groups under which feedback control can be identified. The first type as described in Whitney [Whitney 77] is damping control. This method uses an inverse damping matrix to transform forces into joint velocity commands. Abramowitz [Abramowitz 84] varied the velocity feedback gains at the joints to achieve his version of damping control without an inverse damping matrix.

Another type of active force control is stiffness control [Salisbury 80]. This method uses proportional gains to realize a linear relationship between position error and commanded force. At a specified position, the desired force is commanded open loop. If the forces are unbalanced, the robot and object (or flexible environment) will move until all forces are equal, or the proportional position error times the specified stiffness exactly cancels the force command.

Impedance control, as described by Hogan [Hogan 85], determines the command forces based on position, velocity, and acceleration deviations. Damping and stiffness matrices are used to convert these errors into actuator commands. This method combines the advantages of both the damping and stiffness methods described above.

The fourth type of force control is hybrid position/force control [Raibert and Craig 81]. Two control systems are used simultaneously to close both position and force control loops. This is a very accurate method when both the position and force need to be controlled precisely.

The placement of the force sensor(s) plays a major part in the choice of control scheme. Raibert and Craig used the Scheinman sensing wrist in their hybrid position/force control loops. Salisbury [Salisbury 80] added a deadband to reduce limit cycling and nonlinear limiting to minimize loop gain due to large force errors resulting from impacts. The Jacobian transform was used to resolve wrist forces into joint torques.

Several studies have shown that locating the force sensor on the end effector is unstable when in contact with a stiff environment. Whitney [Whitney 77] showed that the stability was dependent on the compliance between the sensor and the environment. In the case

of a very stiff environment, the sensor should be covered with a compliant surface. An [An 86] supported this by modeling the force control loop as a high gain position feedback scheme. The compliant cover on the sensor would lower the effective gain and therefore increase stability.

In other research [Eppinger 87], the manipulator dynamics between the sensor and the actuators added poles to the system and often led to instabilities. These dynamic effects could be removed by colocating the sensor and actuator, and closing joint torque loops rather than endpoint force loops. An [An 86] suggested a combination of joint and endpoint sensing. The joint torque control would be used for stable dynamic behavior, and the force sensor would provide higher steady state accuracy.

Joint torque sensors have also been shown to increase the system bandwidth. Wu and Paul [Wu 80] used a linear model on a single link manipulator with joint sensing. The analog hardware closed the loop directly around the joint, avoiding the calculations associated with the Jacobian. This allowed a much higher bandwidth with very fast response. Luh, Fisher, and Paul [Luh 83] extended this analysis to include the first two joints of the Stanford Scheinman manipulator. They modeled each joint as a linear system with a backlash nonlinearity for the harmonic drive.

Cannon and Rosenthal [Cannon 84] investigated manipulators with non-colocated actuators and sensors. While stable control loops were easily obtained for colocated sensors, it was much more difficult when the sensors and actuators were non-colocated, especially in a flexible system. This research was extended [Tilley 86] with the addition of a fast end-effector to a flexible manipulator. The wrist subsystem employed its own

force loop upon contact. This force controller recognized movement of the main link as a disturbance and improved the response of the flexible manipulator.

Several other researchers designed arms specifically for force control. Asada and Kanade [Asada, Kanade 81] designed a direct drive arm to eliminate transmission backlash and reduce limit cycling. Youcef-Toumi [Youcef-Toumi 87] showed that the decoupled dynamics of his direct drive arm greatly simplified the computations required for surface following. As with other direct drive manipulators, this design exhibited fast actuator dynamics, low friction, and no mechanical backlash.

1.1.2 Whole-Arm Manipulation

A new area of manipulator research involving force control is *Whole-Arm Manipulation*. First described by Salisbury [Salisbury 87], this method uses all the link surfaces for manipulation, rather than just the end-effector.

Several advantages are gained by using the links in addition to the endpoint. Larger objects can be grasped between the lower and upper links. Large forces can be exerted by moving the center of mass of the object to a point on the arm closer to the base. Collisions can be detected at any point on the device, rather than where the sensor is placed. This type of manipulator would be desirable in an unstructured environment such as space or undersea, where tasks vary widely, and collisions are inevitable. A further extension to the concept of *Whole-Arm Manipulation* would consist of several *WAMs* grouped together to form a much larger manipulator. If each *WAM* also carried a small dexterous hand, the system would be capable of handling objects ranging from very small to those as large as the manipulators themselves.

As described in Salisbury et. al. [Salisbury 88], several things must be taken into consideration when designing a *WAM*. Since the primary application of this system is to manipulate and detect objects in unstructured environments, forces must be controllable anywhere along the links. It is therefore a necessity for the manipulator to have precise and reliable joint torque control and sensing. In order to maximize the contact area of the links, they should be long and narrow, providing a large workspace. The links should also be free of protruding cables and actuators, so as not to interfere with manipulative tasks. To increase speed and payload capability, the motors should be located as close to the base as possible.

In view of these requirements, *Whole-Arm Manipulators* were built at the MIT Artificial Intelligence Laboratory [Townsend 88] and the Woods Hole Oceanographic Institute [DiPietro 88]. The *MIT WAM* (figure 1.1.2) was designed to be inherently force controllable. Its cable transmission is highly efficient, with virtually no friction and zero backlash. The resulting backdrivability makes it possible to sense link forces from motor torques. The links are lightweight with a high aspect ratio. **This high performance manipulator has shifted the limiting constraints on force accuracy and bandwidth from the transmission and structure to the motors.**

The existing *WAM* control system uses commanded motor current to estimate the torque, and provides for feedforward ripple compensation. The sensors, ripple, friction, and other factors limit the open loop torque accuracy to about 8% of full output. Paul [Paul 87] and Eberman [Eberman 89a] used feedforward ripple compensation to reduce the error to about 5%. While this may be acceptable for some feedforward force appli-

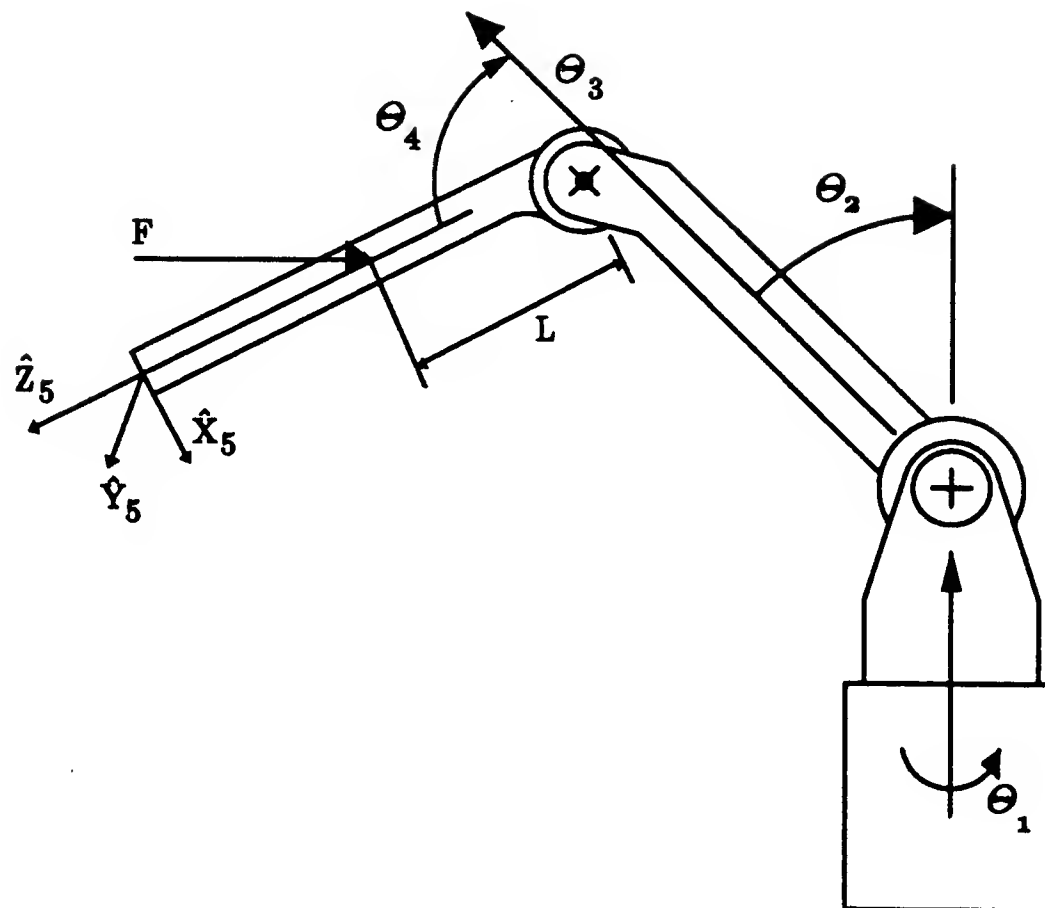


Figure 1.1: The MIT Whole-Arm Manipulator.

cation, it causes significant errors when used for point of collision detection, where poor solution conditioning may require precise torque measurement [Eberman 89b]. Salisbury et. al. [Salisbury 89] discusses the control system and performance of the *MIT WAM*.

1.2 Thesis Overview

The purpose of this research was to develop and implement a torque actuator capable of meeting the performance needs of the *WAM*. The actuator required precise torque control, a large dynamic range, and high bandwidth. Additionally, it had to be physically compatible with the existing manipulator.

Chapter 2 provides some background on torque control, and illustrates some of the popular methods. It also describes some of the theory and analysis that went into the design and choice of the major components. It includes descriptions and tradeoffs of motors, sensors, and controllers.

Chapter 3 presents a brief summary of the actuator design including components, layout, and design requirements/specifications. Controller architecture and software considerations are also included.

Chapter 4 presents a model of the actuator system. The characteristics of DC motors are formulated. Transfer functions for the motor, sensor, and controller are derived. The motor and sensor bandwidths are estimated. Nonlinear disturbances such as torque ripple and friction are also discussed.

Chapter 5 details the performance of the open and closed loop systems. Torque accuracy and bandwidth are discussed in detail. Figures include quasistatic torque output, frequency response, and time response. The effects of torque ripple and friction are also illustrated.

Chapter 6 summarizes the success of this project in meeting its goals. Problem areas and suggestions for improvement are included.

Chapter 2

Torque Control Design Considerations

There exist two basic forms of torque control: open loop control assumes that an accurate model of the system exists and all errors can be minimized using the appropriate feedforward techniques; feedback control, on the other hand, does not require as precise a system model, but utilizes a transducer to determine the torque error.

Open loop torque control does not require a torque sensor, so is generally less costly to implement. For tasks that do not require high torque accuracy, the motor can be modelled as a simple linear gain. Most DC motors have well behaved torque constants over their operating range. For applications where dynamic response or high accuracy is important, an accurate system model is necessary to predict the output torque. Inherent system disturbances such as torque ripple and bearing friction may require nonlinear feedforward control laws. In the case of ripple, a lookup table containing the zero speed ripple as a function of shaft angle is often used. Torque ripple will be discussed in more detail in chapter 4.

Feedback control, on the other hand, does not require an extremely accurate dynamic model of the motor. The output torque can be determined more precisely and fed back for comparison with the command. The controller can then compensate for all the errors simultaneously without distinguishing between the sources.

There are many ways of feeding back the torque information. The least complicated involves measuring the currents flowing to the motor. Since the torque constant makes this a theoretically linear relationship, the actual torque can be observed fairly accurately. Unfortunately, this technique does not include non-linearities such as friction, ripple, and dynamic effects which can typically cause errors of up to 10%. For this reason, feedback of the actual system torque is required.

The introduction of a torque sensor provides precise information about the torque state of the system. The selection of the sensor should be matched to the application for the highest possible bandwidth and resolution. The tradeoffs in sensor designs will be discussed later in this chapter.

2.1 Bandwidth and Dynamic Range

The two most significant factors in designing a torque controller are the system bandwidth and the dynamic range of torque controllability. The bandwidth is a measure of how quickly the system will respond to disturbances or changes in the command. Factors which influence bandwidth include electrical and mechanical time constants, sampling and servo rates, and mass-compliance ratio of the system. The dynamic range is a ratio relating the maximum output torque to the torque precision. This value is dimensionless

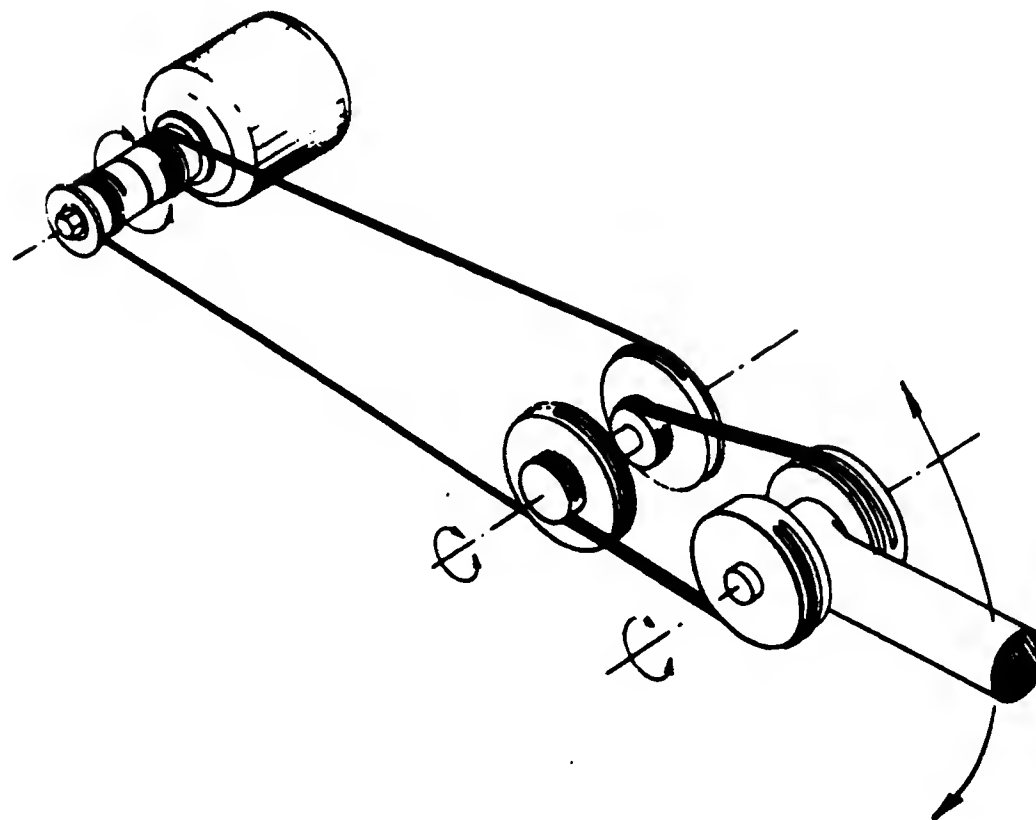


Figure 2.1: A Two Stage Cable Transmission.

and is useful in comparing small actuators with highly accurate torque output against actuators having a wider operating range, but lower accuracy. Both the motor and sensors need to be chosen to satisfy the full range of torques, yet maintain high accuracy and sensitivity. A brief description of the design and characteristics of the *MIT WAM* will provide some performance guidelines.

2.1.1 Whole Arm Manipulator Design

The *WAM* uses a novel cable transmission to link the motors with the joints [Townsend 88]. The two stage configuration also acts as a reduction with ratios of 30:1 in the first three joints and 20:1 in the fourth joint. Where long cable lengths are required, such as in the

fourth joint, the high speed first stage cable is used, as seen in Figure 2.1. The effective stiffness of this cable at the output can be estimated by multiplying the low tension stiffness by the transmission ratio squared. In addition to high stiffness, the cable transmission virtually eliminates the deadband associated with backlash, and has very low friction. Forward and reverse efficiencies are both above 95%, making the arm extremely backdrivable.

Each of the four joints is driven by a Moog 303-003 DC brushless motors. These motors are capable of a torque output of 15 in-lb continuous with peaks up to 60 in-lb. A resolver is mounted on the shaft of each motor for position and commutation information. The drive pinions affixed to the motor shafts are composed of two halves. One half may be rotated relative to the other to pretension the cables.

The current *MIT WAM* control system uses a form of open-loop torque control. It incorporates some feedforward compensation to reduce the effects of torque ripple and cogging. Unfortunately, the highest accuracy possible with this system is on the order of 5% of full torque. This gives the system a dynamic range of about 20:1. One of the design goals of this research was to improve the torque accuracy to below 1% of full torque, increasing the dynamic range to greater than 100:1. Since this degree of accuracy would be very difficult to achieve with feedforward compensation (due to high order ripple harmonics, bearing stiction, and other time-varying and nonlinear effects), the design effort was focused on a feedback system utilizing a torque sensor.

Eberman [Eberman 89a] measured the stiffness of the transmission. He found that the stiffness at the motor of the cables in the fourth link were approximately 40 in-

lb/rad. The effective stiffness is increased by the square of the transmission ratio to 16,000 in-lb/rad at the joint. Since this joint has the longest free length of cable, all of the other joints will have a slightly higher stiffness. Eberman also measured the natural frequencies of the manipulator in free vibration. The fourth link, although it had the lowest stiffness, had the highest natural frequency, at 56 Hz, due to its extremely low mass. This is the resonant frequency of interaction between the motor and the link mass through the transmission stiffness. The damping ratio was found to be about 0.3. Since these tests were conducted, the last link has been replaced with one having about 3 times the mass of the original, which would lower the natural frequency significantly. The natural frequency of the base joint was observed to be 44 Hz, which is the lowest of the four, and had a damping ratio near 0.6. The implemented control system was capable of obtaining a closed loop natural frequency of 2 Hz with a damping ratio of 0.5 under position control.

2.1.2 Actuator Design Goals

Based on the *WAM* characteristics, some basic guidelines were developed for the actuator:

Continuous output torque:	± 15 in-lb
Torque accuracy:	≤ 0.15 in-lb
Bandwidth:	≥ 100 Hz.
Diameter:	≤ 3.00 in
Length:	≤ 7.00 in

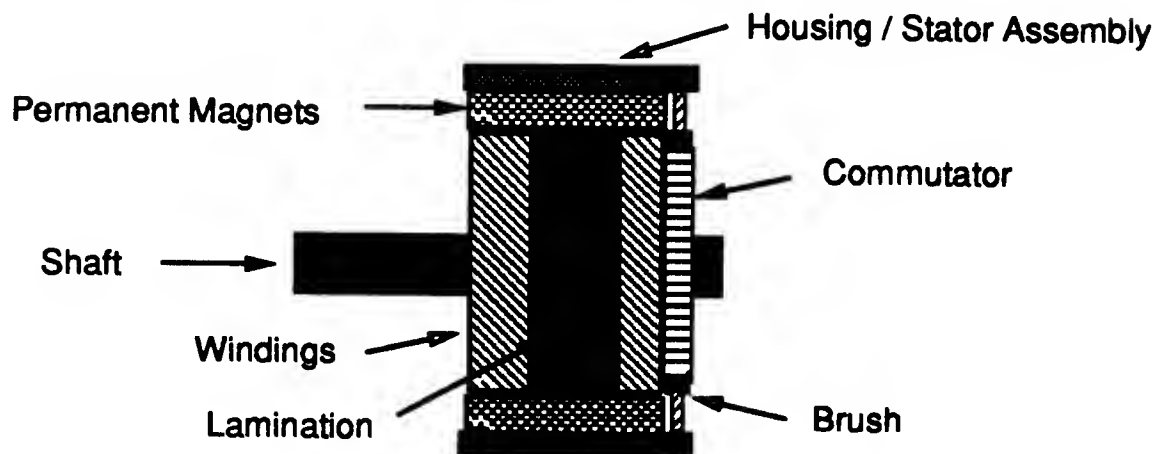


Figure 2.2: Conventional DC Motor Layout.

These baseline figures assure compatibility with the *WAM*, and enable the system to detect all torque variations below the manipulator natural frequencies.

2.2 Design Options

This section will discuss some of the various technologies that could be used in the development of the actuator. The characteristics of each will be examined to determine if it will satisfy design guidelines and provide robust, accurate torque control.

2.2.1 Motor Selection

The first decision that must be made when choosing an electric motor is whether it has brushes or is electrically commutated. This section will describe both types of motor and present the benefits and disadvantages of each.

Conventional DC motors are constructed with permanent magnets on the stator, phase windings on the rotor, and internal commutation brushes to mechanically switch motor current. By moving with the rotor, the commutation brushes effectively maintain

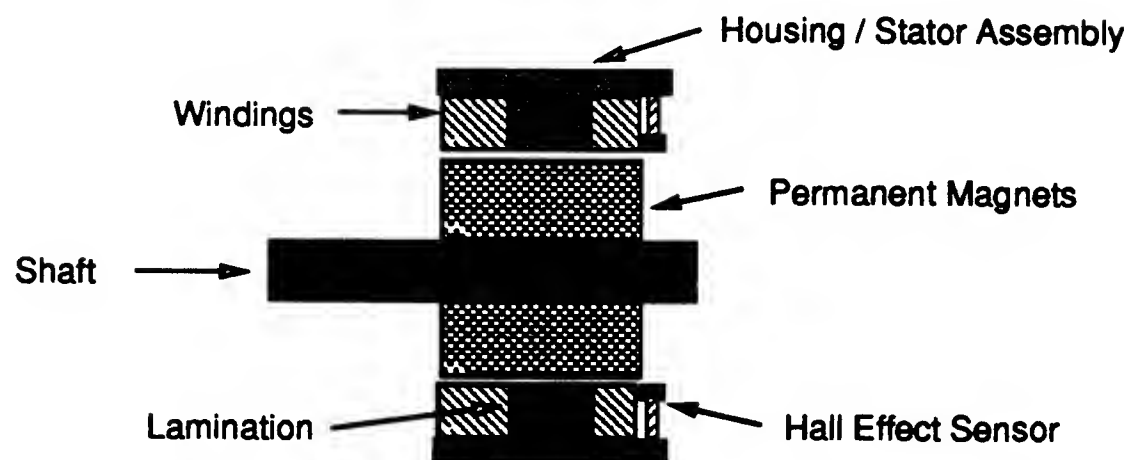


Figure 2.3: Brushless DC Motor Layout.

a stationary rotor current field, properly aligned with the stator magnetic field, regardless of rotor position. Torque is produced by the interaction of the permanent magnet induced flux with the phase winding current vector. The layout of a typical DC brushed motor can be seen in figure 2.2.

A brushless motor is essentially an 'inside out' brushed motor. The phase windings are located on the stator, with the permanent magnets mounted on the rotor. Commutation is achieved by alternately energizing the motor phases through electronic switching. The rotor position is required to smoothly commutate the motor. Several feedback devices can be used for this purpose: Hall effect sensors, resolvers, and encoders. Many brushless motor drivers use current feedback to accurately control the current flow to the motor. Commutation schemes can be as simple turning the phases on and off when the magnets are in the correct orientations, to continuously varying the current to each phase. The latter method is referred to as sine-wave commutation, and produces a significantly smoother torque than trapezoidal commutation. A layout of the basic components of a brushless motor can be seen in figure 2.3.

The following motor characteristics are pertinent to this application:

- **Brush friction-** as a result of mechanical commutation, there is a measurable friction in brushed motors. The only friction in brushless motors is due to the bearings. The amount of static friction in the motor will affect its torque deadband and limit its accuracy.
- **Switching noise-** brushed motors radiate large amounts of electrical noise as the brushes contact the commutator segments. The frequency of this noise is proportional to the speed of the motor. Brushless motors exhibit switching noise at the controller as each phase is energized. Very high frequency noise occurs if Pulse Width Modulation is used, due to the transistors switching state.
- **Thermal Constant-** Since the windings on a brushed motor are on the rotor, its heat is dissipated primarily by convection. Brushless motors, on the other hand, have their coils on the stator. This allows them to cool through conduction and convection, enabling them to run longer before heating up.
- **Phase number-** brushed motors typically have from 2 - 12 electrical phases. Each is simply a coil wound on the rotor laminations. Brushless motors, however, rarely have more than three phases. The reason for this is that each phase requires its own dedicated power circuitry to correctly commutate it. While winding a few extra coils is relatively inexpensive, adding three more phases to a brushless motor may double or triple the cost of the drive electronics. The number of phases can significantly affect the amount of ripple in a motor. In trapezoidal or brushed commutation, the phase current is constant for a finite angle. The flux density, however, varies as the rotor moves relative to the

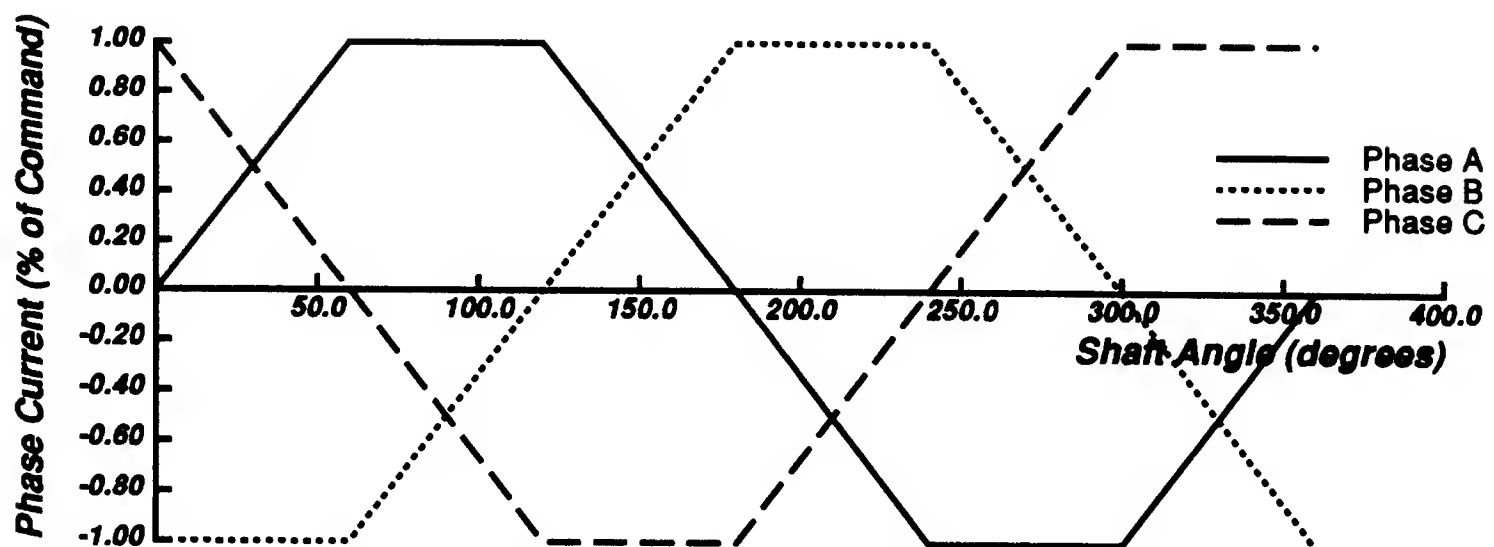
stator, producing a fluctuating torque. The greater the distance between phases, the greater the ripple. Hence, a motor with 6 phases will have inherently less ripple than an otherwise identical motor with 3 phases.

- Pole number - not to be confused with phases, poles are the permanent magnets mounted on the stator of a brushed motor or the rotor of a brushless motor. As with phases, a larger number of poles will tend to reduce the magnitude of the torque ripple. The pole number affects the commutation by requiring the phases to be switched more rapidly and/or interspersed around the motor.

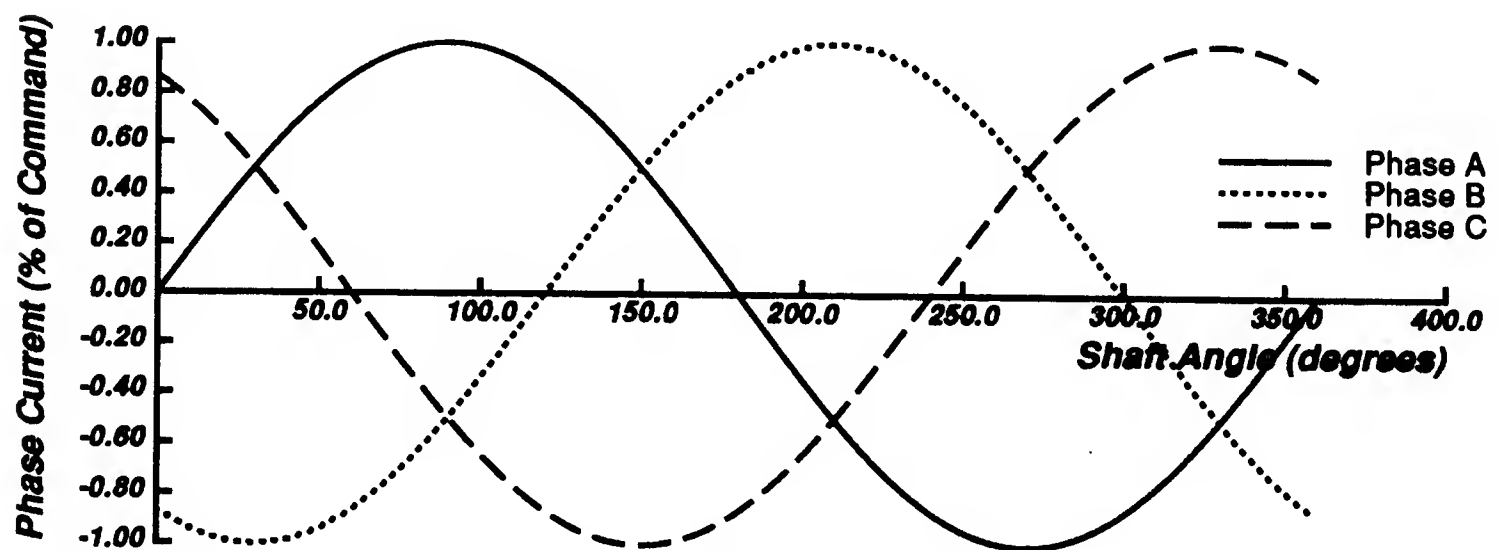
In the end, the brushless technology was chosen primarily to eliminate the effects of brush friction on output torque. The higher thermal time constant also allowed a slightly smaller motor to be used without fear of heating up the coils to their melting point. The absence of electrical arcing across the brushes also make brushless motors preferable for space operation, a probable application of *WAM* technology.

Once the decision was made to use a brushless motor, a choice had to be made between trapezoidal or sine wave commutation. Trapezoidal commutation is far simpler, with the stator coils being alternately energized with the full desired current. An encoder or hall effect sensor is adequate for determining when to switch the phases. Since the phases ramp up and then level out linearly, the magnetic field density varies as the magnets rotate, increasing the effect of torque ripple, and decreasing motor efficiency.

A sine wave commutation scheme, on the other hand, varies the current to each phase continuously as the motor rotates. An EPROM lookup table is used to coordinate the resolver data with phase energization current. Theoretically, perfect sine wave commu-



Phase Current versus Position for 3 Phase Trapezoidal Commutation



Phase Current versus Position for 3 Phase Sine Wave Commutation

Figure 2.4: Comparison of Trapezoidal and Sine Wave Commutation.

tation would yield zero torque ripple, as the magnetic field density is always constant. In practice, however, unbalanced phase gains, offsets, imperfect commutation tables, geometric non-linearities in the magnetics, and out-of-phase resolvers can cause substantial variations. Figure 2.4 shows both trapezoidal and sine wave commutation schemes.

2.2.2 Sensor Criteria

The majority of torque sensing configurations fall into three categories: reaction, inline, and joint mounted. Each technique has tradeoffs to be considered for the particular application.

Reaction sensing: In a typical scheme using reaction torque sensing, the sensor is placed between the actuator and ground. The output from the actuator goes through the transmission to the load, while an equal and opposite reaction force acts upon the sensor. The motor housing is mounted on bearings to isolate the sensor from tangential and axial loadings. The sensor is essentially a strain-gauge instrumented torsion beam connecting the actuator to ground.

A model of a reaction torque sensor is shown in figure 2.5. The simplified equations of motion for this system are:

$$\begin{bmatrix} J_h + J_s & 0 & 0 \\ 0 & J_m & 0 \\ 0 & 0 & J_j \end{bmatrix} \begin{bmatrix} \ddot{\theta}_s \\ \ddot{\theta}_m \\ \ddot{\theta}_j \end{bmatrix} + \begin{bmatrix} 2B_m + B_s & -2B_m & 0 \\ -2B_m & 3B_m & 0 \\ 0 & 0 & B_j \end{bmatrix} \begin{bmatrix} \dot{\theta}_s \\ \dot{\theta}_m \\ \dot{\theta}_j \end{bmatrix} + \begin{bmatrix} K_s & 0 & 0 \\ 0 & K_t & -NK_t \\ 0 & -NK_t & N^2K_t \end{bmatrix} \begin{bmatrix} \theta_s \\ \theta_m \\ \theta_j \end{bmatrix} = \begin{bmatrix} T_m \\ T_m \\ T_j \end{bmatrix} \quad (2.1)$$

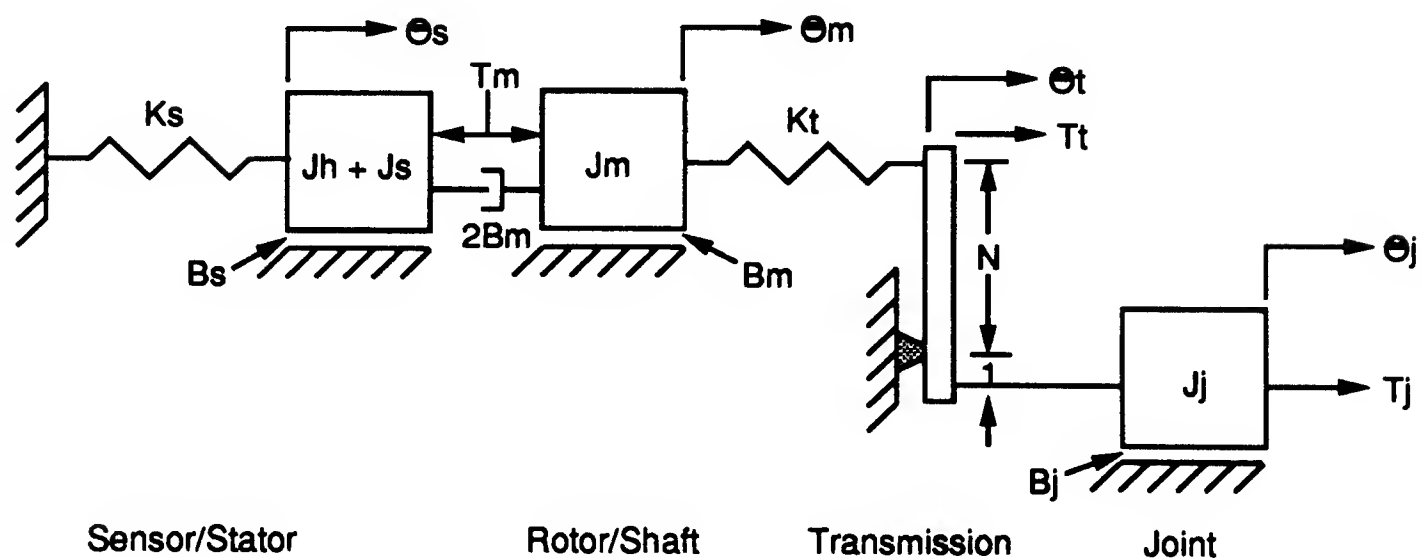


Figure 2.5: Reaction Torque Sensor - Lumped Parameter Model.

where T_m = motor torque	θ_s = sensor angle of rotation
T_j = joint output torque	θ_m = motor shaft angle of rotation
J_h = motor housing inertia	θ_t = transmission angle of rotation
J_s = sensor inertia	θ_j = joint angle of rotation
J_m = rotor/shaft inertia	B_s = inner housing bearing friction
J_j = joint/link inertia	B_m = shaft bearing friction
K_s = sensor compliance	B_j = joint friction
K_t = transmission compliance	

If $B_m \ll 1$, the sensed torque T_s is mechanically decoupled from the last link, leaving:

$$T_s = K_s \theta_s = T_m - (J_h + J_s) \ddot{\theta}_s - B_s \dot{\theta}_s \quad (2.2)$$

The undamped natural frequency between the motor and the sensor is then:

$$\omega_n^2 = \frac{K_s}{J_h + J_s} \quad (2.3)$$

To find the natural frequency between the motor and the system, it is necessary to reflect the joint inertia and friction into the motor domain. This introduces a factor of $\frac{1}{N^2}$ since all forces are reduced by the ratio N , and $\theta_l = \frac{\theta_t}{N}$. However, the torque only gets scaled by $\frac{1}{N}$. Replacing this in 2.1 and removing the decoupled first row:

$$\begin{bmatrix} J_m & 0 \\ 0 & \frac{J_j}{N^2} \end{bmatrix} \begin{bmatrix} \ddot{\theta}_m \\ \ddot{\theta}_t \end{bmatrix} + \begin{bmatrix} B_m & 0 \\ 0 & \frac{B_j}{N^2} \end{bmatrix} \begin{bmatrix} \dot{\theta}_m \\ \dot{\theta}_t \end{bmatrix} + \begin{bmatrix} K_t & -K_t \\ -K_t & K_t \end{bmatrix} \begin{bmatrix} \theta_m \\ \theta_t \end{bmatrix} = \begin{bmatrix} T_m \\ T_t \end{bmatrix} \quad (2.4)$$

To find the undamped natural frequency, take the determinant $|K - J\omega^2| = 0$, and solve:

$$\omega_n^2 = K_t \left(\frac{1}{J_m} + \frac{N^2}{J_j} \right) \quad (2.5)$$

The advantages represented by a reaction sensor include its compact size (less than 1 inch wide) and simple design. Since the sensor is fixed to ground, it has no moving parts, and the shaft is displaced only a fraction of a degree (θ_s). It exhibits a high stiffness proportional to its load range. For robotic applications, the sensor would be colocated with the motor, resulting in a stable direct coupled system. This can be seen in 2.2 where only the stator and sensor friction and inertia terms affect the sensed torque. Mounting on the base of manipulator also means that there is less mass on the outer links, resulting in higher accelerations and forces. The biggest disadvantage with using a reaction sensor is that the sensor is coupled with the stator and motor housing. This large mass (J_h)

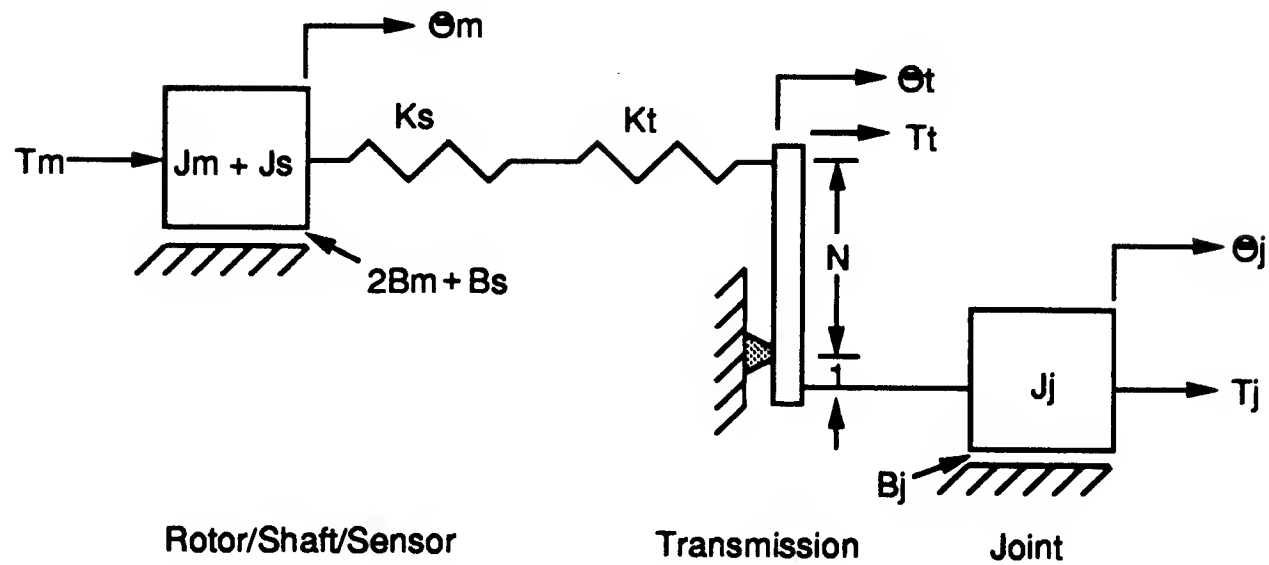


Figure 2.6: Inline Torque Sensor - Lumped Parameter Model.

limits the bandwidth of the system. Additionally, the torque delivered to the joint is not precisely known, since transmission friction and dynamics are between the joint and sensor as seen in figure 2.5.

Inline sensing: The sensor is placed between the rotor and the output shaft. The most commonly used (and least expensive) type are strain-gauge based sensors, where an instrumented torsion bar spins with the motor velocity. A slip ring picks the torque signal off of the rotating shaft. Other types of inline sensors include rotary transformers, torsional variable differential transformers (TVDT), and phase shift devices. These devices can often produce accuracies as high as the strain gauge sensors, but exhibit lower noise rejection and poorer DC response.

A model of an inline torque sensor is shown in figure 2.6. The motor/sensor masses and frictions and sensor/transmission stiffnesses can be lumped together, so the equations

of motion for this system reflected to the motor side of the transmission are:

$$\begin{bmatrix} J_m + J_s & 0 \\ 0 & \frac{J_j}{N^2} \end{bmatrix} \begin{bmatrix} \ddot{\theta}_m \\ \ddot{\theta}_t \end{bmatrix} + \begin{bmatrix} 2B_m + B_s & 0 \\ 0 & \frac{B_j}{N^2} \end{bmatrix} \begin{bmatrix} \dot{\theta}_m \\ \dot{\theta}_t \end{bmatrix} + \begin{bmatrix} \frac{K_s K_t}{K_s + K_t} & \frac{-K_s K_t}{K_s + K_t} \\ \frac{-K_s K_t}{K_s + K_t} & \frac{K_s K_t}{K_s + K_t} \end{bmatrix} \begin{bmatrix} \theta_m \\ \theta_t \end{bmatrix} = \begin{bmatrix} T_m \\ T_t \end{bmatrix} \quad (2.6)$$

The undamped natural frequency for this system is similar to that obtained in 2.5:

$$\omega_n^2 = \frac{K_s K_t}{K_s + K_t} \left(\frac{1}{J_m + J_s} + \frac{N^2}{J_j} \right) \quad (2.7)$$

Since the sensor is now located inline with the transmission, its bandwidth is now limited by the link natural frequency. This has also been degraded by introducing the additional sensor compliance into the transmission. The effect of K_s on the bandwidth can be seen in the stiffness term of ω_n .

Like the reaction sensor, an inline sensor can be mounted on the base of the manipulator, keeping its mass away from the endtip. For very stiff transmissions, when $K_t \gg K_s$, high bandwidths can be achieved, perhaps even better than the reaction sensor, since $J_m < J_h$. The problems inherent with using an inline sensor include noise and brush friction introduced through the slip rings of a strain gauge system, and a lower stiffness than comparable reaction sensors. The other sensor types avoid the slip rings, but also have noise problems which limit their accuracy. The complexity of the sensor is higher due to the moving shaft, and it must be cleaned and lubricated periodically. The package size is usually larger for a given torque range, since it may also include bearings in addition to the sensor and slip rings. Like the reaction sensor, the inline can not observe transmission losses and cannot predict joint torques accurately.

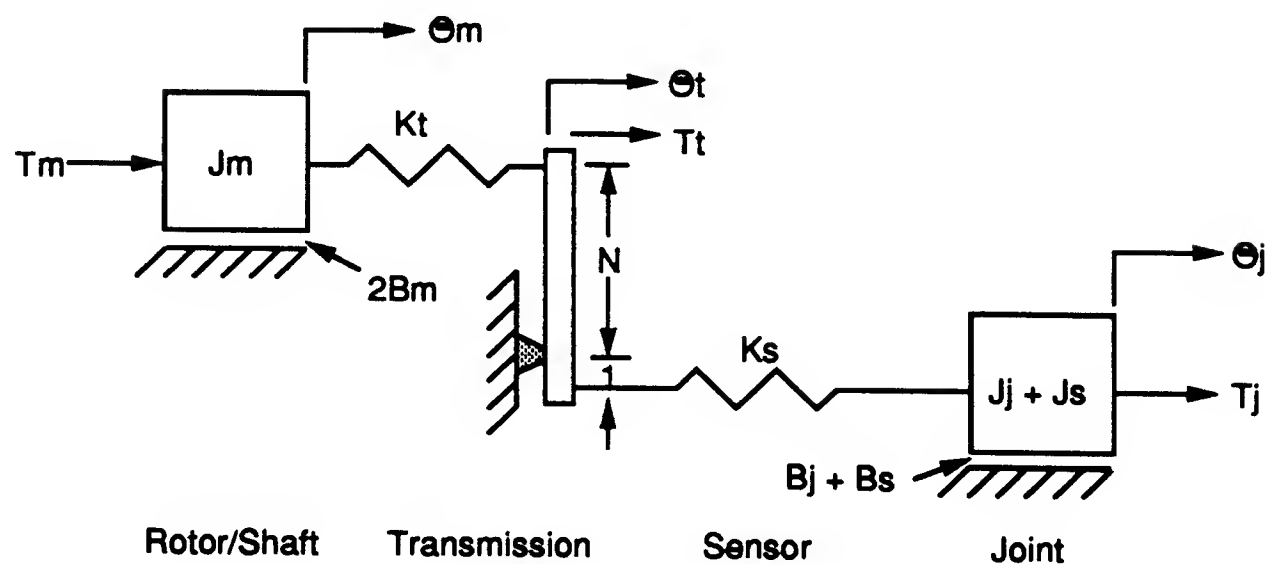


Figure 2.7: Joint Torque Sensor - Lumped Parameter Model.

Joint Sensing: The torque sensor is placed between the output side of the transmission and the driven joint. Alternatively, the joint itself can be instrumented if it is compliant enough to be used as a sensor. Figure 2.7 shows a model of a joint sensor.

When the sensor is moved to the right of the transmission, it is reflected back similar to the joint inertia: $K_s(\text{joint}) = \frac{K_s}{N^2}(\text{motor})$ The equations of motion are modified to be:

$$\begin{bmatrix} J_m & 0 \\ 0 & \frac{J_j + J_s}{N^2} \end{bmatrix} \begin{bmatrix} \ddot{\theta}_m \\ \ddot{\theta}_t \end{bmatrix} + \begin{bmatrix} 2B_m & 0 \\ 0 & \frac{B_j + B_s}{N^2} \end{bmatrix} \begin{bmatrix} \dot{\theta}_m \\ \dot{\theta}_t \end{bmatrix} + \begin{bmatrix} \frac{K_s K_t}{K_s + N^2 K_t} & \frac{-K_s K_t}{K_s + N^2 K_t} \\ \frac{-K_s K_t}{K_s + N^2 K_t} & \frac{K_s K_t}{K_s + N^2 K_t} \end{bmatrix} \begin{bmatrix} \theta_m \\ \theta_t \end{bmatrix} = \begin{bmatrix} T_m \\ T_t \end{bmatrix} \quad (2.8)$$

with a natural frequency of:

$$\omega_n^2 = \frac{K_s K_t}{K_s + N^2 K_t} \left(\frac{1}{J_m} + \frac{N^2}{J_j + J_s} \right) \quad (2.9)$$

It can be seen from the model that the bandwidth limitation is still the natural frequency of the transmission path. This bandwidth is degraded even more than the inline model, since the sensor compliance is reflected through the reduction. This results in the N^2 term in the denominator of the stiffness term.

The greatest advantage obtained by placing the sensor at the joint is that it registers the actual joint torque, including transmission losses. This is the most accurate way to measure joint torques, but also has its disadvantages. The sensor must be mounted directly to the joint, necessitating a larger structure with increased mass. All motors and structures further back in the kinematic chain must then be sized for this greater mass. All power and signal cables would need to run through the links, increasing joint design complexity and maintenance difficulty. From the control perspective, stability at high gains will be difficult to achieve and limit cycling may occur since the transmission dynamics are between the actuator and sensor.

Endpoint mounted force/torque sensors have similar characteristics to the joint sensor. By coming into direct contact with the work, they provide very accurate and high bandwidth information about the actual forces exerted by the arm. Unfortunately, since the sensor is located after the transmission and links, the manipulator dynamics make it very difficult to close a stable control loop about this force. The bandwidth of this controller is therefore limited by the natural frequency of the arm. In very stiff, low inertia mechanisms the upper frequency bound is on the order of 50 Hz, and can fall as low as 1 or 2 Hz for very flexible structures.

After comparing the advantages of each sensor class, it was decided to use a reaction

torque sensor. The primary reason for its selection is that, for relatively compliant transmissions (such as found in the *WAM*), the reaction torque sensor provides the highest motor - sensor bandwidth. High bandwidth is far more important in *Whole Arm Manipulation* applications than accurate joint torque control, due to the stiffness control scheme utilized. In this controller, the torque is computed from the position error scaled by a stiffness gain matrix. Since the transmission is greater than 95% efficient, the motor torque is a very accurate representation of the actual joint torque. We felt it was far more important to improve the accuracy of the torque generated by the motor, since all torque errors would be scaled by N at the joint. This required the high bandwidth obtainable only with the reaction sensor. Additionally, the insertion of either an inline or joint sensor between the motor and joint would add more compliance, thus degrading the position bandwidth.

The reaction torque sensor is also the smallest of all the devices. It can be located inside the actuator, producing a clean compact package that can be mounted to the base of the manipulator. This would also eliminate routing additional signal wires through the arm, simplifying assembly and maintenance.

Chapter 3

Design

3.1 Hardware Design

There are three main components to this system: the actuator package, drive electronics, and torque controller. The following sections will briefly describe the design and capabilities of these modules. Appendix A contains the machined parts drawings, and appendix B includes data sheets for the actual components.

3.1.1 Actuator

The actuator mechanism consists of a frameless torque motor, modular resolver, and reaction torque sensor, as seen in figure 3.1. As explained in chapter 3, the motor is a three-phase brushless DC motor, with rare-earth magnets for high flux density. Baseline design requirements include a continuous torque of 15 in-lb at a speed of 2500 rpm. HHK Industries has customized a motor to meet these requirements.

The resulting motor has a diameter of 2.5 inches and stack length of 2.5 inches. Unlike most brushless motors, this model is 'slotless'. Instead of wrapping the coils around an

iron core to concentrate the magnetic field, the stator is filled completely with wire. Flux density is higher despite an airgap that is much larger than found in conventional motors. The extra room for windings allows larger coils to be used, resulting in lower copper losses and a higher thermal time constant. The motor inductance is also much lower than that of motors containing toothed-type stators. Iron losses and cogging are common in conventional motors and result from the changing reluctance in the magnetic paths between various points on the magnets and stator. The reluctance is much lower in the magnetic paths between the magnets and the teeth than in the paths between the magnets and the stator through the slot openings. Another characteristic of toothed motors is a varying flux level in the teeth as the motor rotates. This varying flux can cause hysteresis and eddy current losses, which may account for more than half of the losses in a conventional brushless motor. The resulting efficiency from this motor is significantly higher than that of a comparable slotted motor. Cogging is also virtually eliminated.

The rotor is composed of six rare-earth magnetic poles arranged hexagonally on a stainless steel insert. The inner diameter of the rotor contains a keyway for mating to the shaft. Unfortunately, keys permit a small amount of misalignment and backlash, and were therefore unacceptable in this design. The solution was to knurl the shaft to a slightly larger dimension than the the rotor inner diameter. This shaft could then be press fit into the rotor with the knurled section providing more compliance than the solid shaft. This method assured concentricity and avoided backlash completely.

The motor housing is essentially a thin walled aluminum cup with a precision instru-

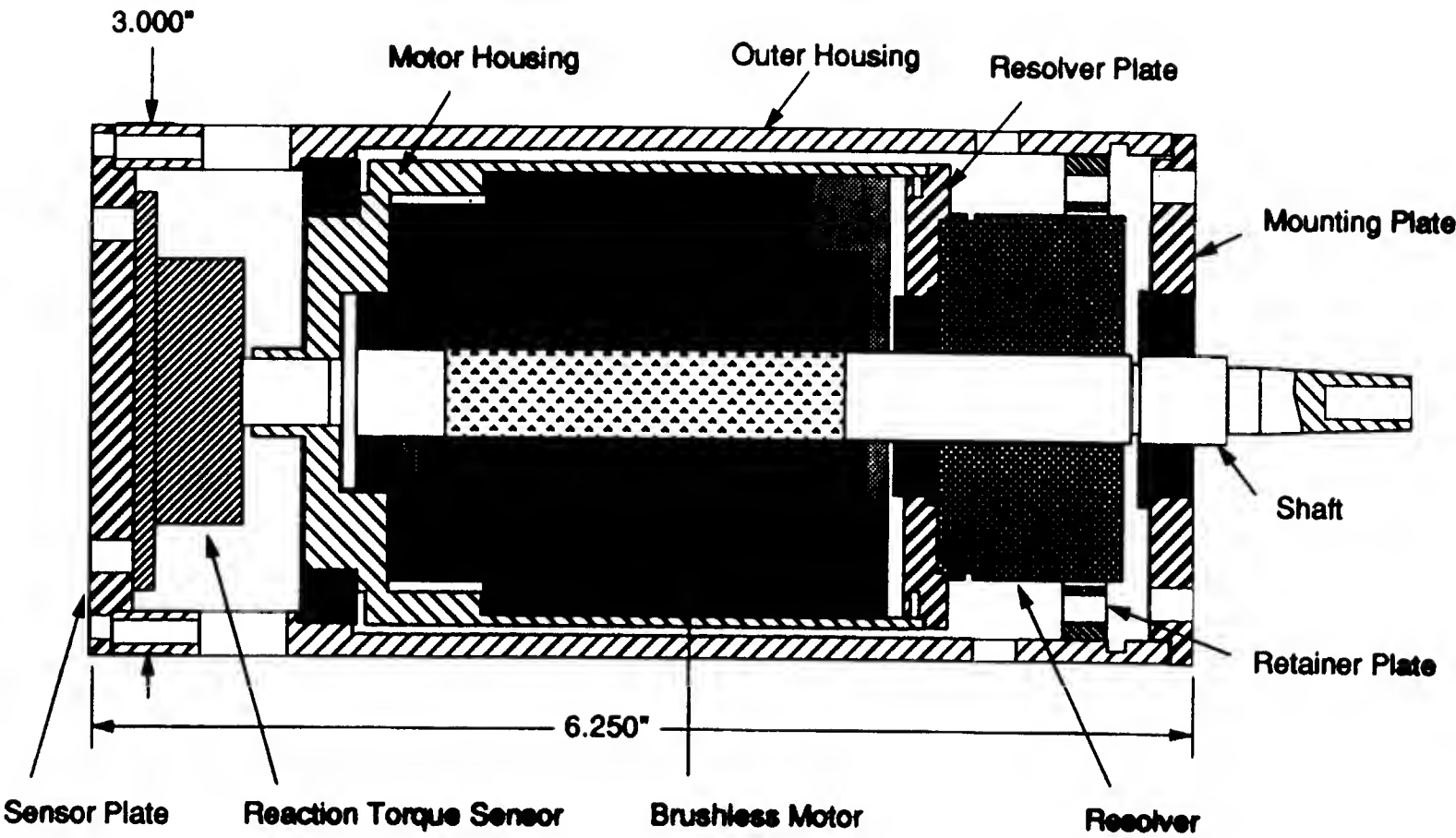


Figure 3.1: Actuator layout.

ment bearing centered on its bottom. The stator assembly was first given a coating of thermal grease and then slid in until the laminations made contact with a small shelf. A silicon rubber adhesive sealant was used to bond the stator to the housing. A thin bearing plate was mated with the open end of the motor housing, and aligned with two slots. Pins were inserted through these slots into the plate to keep it from moving relative to the housing.

A modular resolver is attached to this housing on the output end, with the shaft running through its center. This resolver is a single speed transmitter model produced by Clifton Precision. Its brushless design minimizes friction while providing an accuracy of 15 arc minutes. Encoders were investigated as an alternative, but could not be used by the motor controller for sine wave commutation. Servo mount cleats were used to attach the resolver to the plate and enable accurate phase adjustment. Precision shaft spacers were inserted on both sides of the resolver rotor to properly position and preload the shaft against the housing bearings.

The motor housing is suspended inside the outer housing by two bearings. A Kaydon Reali-Slim bearing is press fit onto the back of the cup, and rests on a flange in the outer housing. The other bearing is mounted on the shaft at the point where it exits the housing. The bulkhead containing this bearing required a special design, since the thin housing walls did not permit axial screws. As this was also the mounting surface, it needed to be a strong, reliable connection. The design required that a groove be cut into the inside of the housing. An internal snap-ring fit in this groove and retained a plate. The bulkhead was then screwed into this plate and tightened against the snap-ring. This

arrangement provided a very strong, positive connection.

Mounted to the back motor end plate is the input shaft of a reaction torque sensor. This strain gauge based sensor is made by Sensotec and boasts a range of 50 in-lbs with linearity to 0.1%. Deflection at full load is less than 0.25 degrees of arc. The sensor itself is mounted to the rear bulkhead of the outer housing by six screws. The motor housing is mated to the sensor input shaft by a collet and compression clamp. This coupling is preferred over the traditional set screws because it eliminates backlash and does not cause surface stresses on the shaft. Since the motor housing is supported by the Kaydon and shaft bearing, the torque sensor is effectively isolated from radial and axial loading.

The operating concept of the torque sensor is essentially a torsion bar instrumented with strain gauges. Due to the very low output voltages from strain gauges (on the order of millivolts), it is necessary to mount an instrumentation amplifier and low pass filter assembly near to the motor housing. The amplifier and filter raise the signal to noise ratio, and hence improve torque resolution. An Analog Devices 5931B Strain Gauge Signal Conditioner, a 28 pin DIP, was used. It contains a full bridge strain gauge instrumentation amplifier and second order low pass filter. The cutoff frequency of the filter can be adjusted from 10 Hz to 20kHz. This circuit and compensating resistors and capacitors are mounted in a shielded metal box in close proximity to the torque sensor.

3.1.2 Drive Electronics

The incorporation of a strain gauge based torque sensor into the actuator package places severe constraints on the motor drive electronics. The amplifier output should be virtually DC, as high frequency noise would corrupt the millivolt strain gauge signals. Unfortu-

nately, most pulse width modulated amplifiers radiate voltage spikes at their switching frequency. The drivers used in the current WAM system produce up to 12 volt 2 MHz spikes every 0.2 msec, which can be detected virtually anywhere in the lab. This noise is certainly large enough to trip TTL logic, and would easily eradicate a low voltage torque signal.

There were two possible solutions to this problem. The first was to find or design a linear amplifier capable of driving the chosen motor. This would eliminate high frequency noise at the source, since there is no switching component. Unfortunately, there are not many linear amplifiers capable of driving a 3 kilowatt load, and even fewer are configured for brushless motors, as this would require three individual linear power stages. In general, linear amplifiers are not used very frequently because they need to be much larger than comparable PWM amps, and are much less efficient, dissipating the losses as heat.

The other possibility for a low noise high power servo amplifier was to go with a PWM design that uses low pass filters on the output stage. These amplifiers meet military specifications for EMI/RFI, and consequently are about twice as expensive as other brushless amplifiers. Unfortunately, the only company producing these Mil-spec amplifiers does not yet have a version for sine wave commutation.

Faced with these conflicting constraints, the only alternative was to attempt to minimize the switching noise. This was accomplished by boosting the PWM frequency to 16 kHz, using sine wave commutation, and heavily shielding the motor and cabling. It was left to the instrumentation amplifier to filter and increase the signal to noise ratio

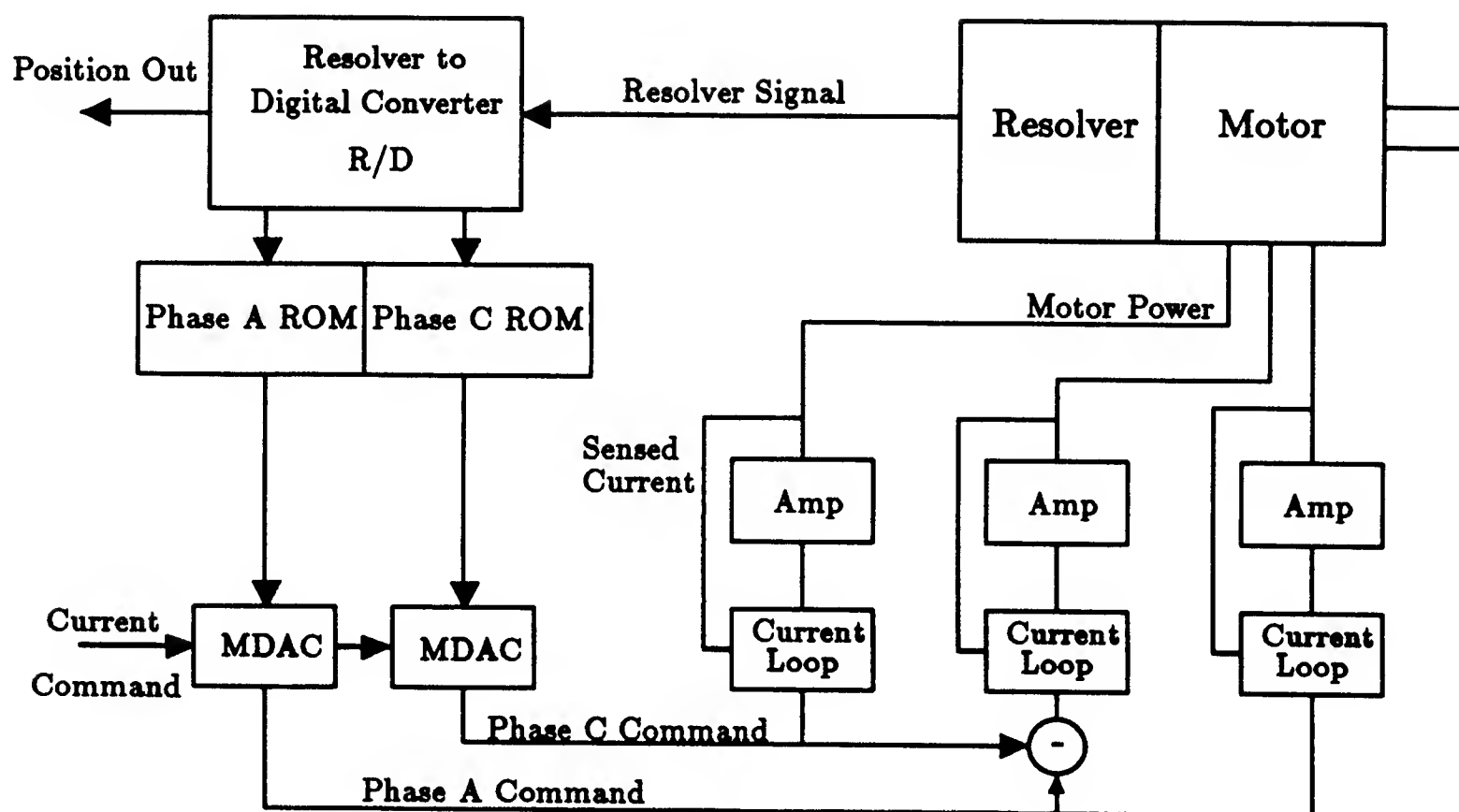


Figure 3.2: Functional Layout of a Brushless Motor Controller.

to a point where the remaining noise would be insignificant. Final filtering and noise rejection was also implemented in software.

The drive electronics selected for this actuator are made by Infranor. Figure 3.2 shows a functional block diagram of the motor control electronics. An internal resolver to digital converter interprets the resolver output as shaft position with a resolution of 12 bits. A sine wave commutation table translates this position into the correct current for each phase. A current loop is closed around each phase to improve torque accuracy. The analog input range extends to ± 10 volts, with full scale producing 10 in-lb of torque.

3.2 Development System

The motor controller reads and processes all inputs, closes the low level torque loop, and outputs motor commands and position/velocity data. For initial development, the Condor multiprocessor system was used to provide the necessary hardware and software interface. Eventually, each actuator will be driven through its own control module, freeing up the Condor for higher level tasks.

The inputs to the controller include the commanded torque, resolver data, and the torque sensor signals. Optional inputs include motor temperature and current. The input processing includes analog to digital conversion, signal filtering, position tracking, and velocity calculations.

3.2.1 Condor Hardware

The control implementation for the actuator shares the Condor environment of the *MIT-WAM*. This system consists of five Ironics 3201 single-board computers, an Ironics 3273 Bus Controller, a Data Translation 1401 analog-to-digital converter, a Data Translation 1406 digital-to-analog converter, and two Motorola MVME-340 parallel ports. This hardware is housed in a VME-Bus card cage, and interfaced to a SUN-3/280 workstation through a HVE-2000 VME bus-to-bus adapter. The Sun is used for program development and for analyzing data stored on the processors.

The computation in each Ironics 3201 is performed by a Motorola 68020 microprocessor with a 68881 floating point accelerator. One megabyte of dual-ported RAM is contained on each board, and can be accessed by the local CPU or across the VME bus.

The bus controller provides interrupt management, bus arbitration, and reset functions. The DT 1406 D/A board provides eight 12 bit digital-to-analog converters which are used to transmit commands to the motor controllers. The DT 1401 A/D has 32 single-ended analog-to-digital converters with 12-bits of resolution and programmable gains. The Motorola parallel-port boards read the digital position signals from the motor controllers without handshaking, and can be configured for interrupts. Optical isolation is provided between the amplifier and the DIO board to eliminate the electromagnetic noise radiated by the pulse width modulation. The HVE bus connector links the Sun directly to the VME bus, allowing it to access the dual ported RAM on the processors.

Since the system is only required to control a single axis, it was possible to achieve sufficient computational speed using just one of the five processor boards. This board acts as the input/output processor and closes all of the control loops. The A/D board provides feedback from the torque sensor. One of the parallel boards is used to read position data, and motor commands are issued through the D/A board.

3.2.2 Condor Software Support

The Condor system software provides many useful features for real time control. Some of the embedded functions consist of device drivers for the hardware components, a mailbox system for message passing, basic UNIX functions, debugging support, a virtual terminal for each processor, and a large number of user utilities.

The Sun provides the programming and interface environment for the Condor system. Since both the Sun and the Ironics processors are based on the 68020, the standard C compiler can be used. For large tasks, the control code can be split into separate

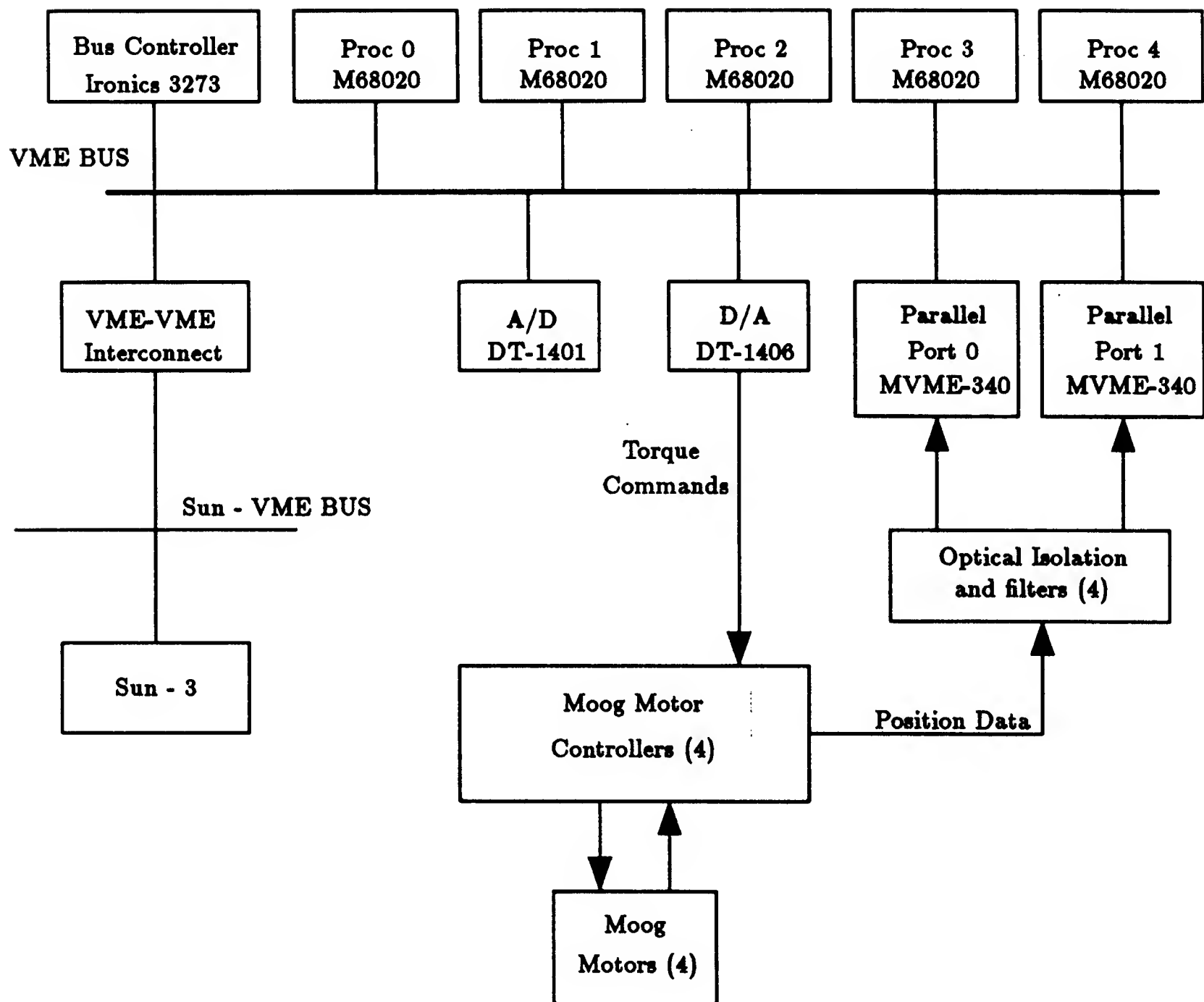


Figure 3.3: MIT-WAM Control Hardware Block Diagram.

programs, each running on its own processor. A real-time library containing UNIX functions and software utilities is linked to each routine. These control programs can then be downloaded to the microprocessors over the bus to bus connector. A virtual terminal connects each of the processors to the Sun so that each board has a window on the workstation. Additionally, the Sun has access to the dual-ported RAM on each processor. There is also a software mailbox system allowing the processors to pass data among themselves.

Some of the utilities offered by the Condor environment include device drivers for all of the input/output boards. There are also special purpose routines developed for servo implementation. The system is capable of looping through a user defined routine at a specified servo rate. Interrupts and error handlers can be defined to kick out of the loop, or execute a different routine. This eases the programming task by embedding the timing and interrupt code in the operating environment.

3.3 Software Implementation

Although the Condor system is capable of supporting five processor boards, only one was required to achieve the desired loop speed. This single processor performed all functions from input processing through motor commands. A command menu was provided to execute individual processes for debugging and evaluation purposes. Print and write routines were available for data collection. Switches were provided to select and enable the control algorithms. A significant amount of the software was adapted from the *WAM* operating system [Eberman 89a][Niemeyer 89] so that the controller would be compatible

for direct motor substitution. Brief descriptions of some of the software routines follow.

A substantial portion of the code is dedicated to input processing. These routines read the parallel port to obtain a digital representation of the resolver position. Absolute position is maintained by counting motor revolutions. These position values are filtered to remove any spurious points caused by motor noise or conversion errors. Since the Condor system does not take advantage of the converter busy signal due to noise problems, errors can be introduced by reading the parallel port in the midst of the conversion. The filtering method compares the last two points with the new input, and takes the median value as the new point. The velocity is then computed using a first order difference and passed through another filter. Both the position and velocity values are stored in local RAM.

Other inputs that require processing include the sensed torque. This value is collected through the A/D convertor, and then converted to usable units using scaled gains and offsets. This value is also similarly filtered to eliminate noise.

Output processing consists of converting the torque specified by the control loop into D/A units and sending it to the DT1406.

A main control menu is included in the software. This menu enables the user to select a control loop, vary the gains, and adjust the servo frequency. Other options include data collection and display, input/output test routines, and status reports. Torque and position commands can also be specified through menu driven input routines. The user can select torque or position, magnitude, and the duration of the move/torque. A model of the controller will be discussed in detail in chapter 4.

Although the prototype system was implemented on a single processor in the Condor

environment, it required a substantial amount of computational power. For a full WAM implementation of four torque controlled actuators, separate controller modules would be required for each motor. Each module would consist of a microprocessor, dual-port dynamic RAM, and all necessary I/O hardware. The processor has not been determined, but will likely be either a standard 16 bit design or a digital signal processing chip. Both options will be explored before a decision is reached. The memory unit should be dual-ported to allow adaptive gain changes and access by the supervisory controller. All communications with the host will be accomplished through a parallel link to provide high speed data transmission. This type of control module would relieve the Condor system of the computational burden of performing the I/O processing and closing the low level torque loops. If a DSP were used, each module would be capable of closing a full impedance controller and performing additional I/O tasks.

Chapter 4

System Model

This chapter will derive the models for the various components that make up the actuator. Disturbances such as torque ripple and friction will be studied. The bandwidth of each component and the entire system will be estimated.

4.1 Motor Model

A model of the basic stator circuit equivalent for a permanent magnet brushless motor is shown in figure 4.1. This is a linearized model of the current in a frame rotating with the motor. This allows the stator to be modeled as an average phase inductance

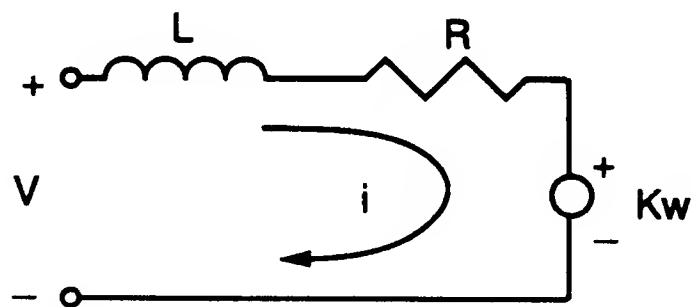


Figure 4.1: Stator Equivalent Circuit.

and phase resistance. In reality, the inductance will vary as the motor rotates and with motor current, and will also include mutual inductance from the other windings. A source voltage V_a drives a current i through this stator winding which develops a torque on the rotor. The inductance and resistance of the windings cause a voltage drop across the coils. If the rotor is free to rotate, it will accelerate to some speed at which its counter-emf is approximately equal to the applied voltage after the drop. This counter-emf generated in the stator windings opposes the applied voltage and balances the electrical and mechanical power. It is proportional to speed ω by the constant K_e . Equation 4.1 shows the effects of the inductance, resistance, and counter-emf on the applied voltage.

$$V_a = L \frac{di}{dt} + Ri + K_e \omega \quad (4.1)$$

Multiplying the above equation by i yields the power in the system.

$$P = V_a i = \frac{1}{2} L \frac{d}{dt}(i^2) + Ri^2 + K_e \omega i \quad (4.2)$$

The first and second terms in equation 4.2 are the power stored in the inductance and dissipated by the resistance, respectively. The final term is the power that is converted into mechanical energy. From conservation of energy, K_e , the back EMF constant, and K_t , the torque constant, are equal, although they have different units. Taking the derivative of motor power, P_m , with respect to ω yields the torque:

$$P_m = T_m \omega = K_e \omega i \quad (4.3)$$

$$\frac{\partial}{\partial \omega} P_m = T_m = K_e i = K_t i \quad (4.4)$$

For a steady state current, the inductance term has no effect. Neglecting the inductance and substituting 4.4 back into 4.1 yields a relationship between torque and speed.

$$T_m = \frac{K_t}{R} (V_a - K_e \omega) \quad (4.5)$$

By setting the torque to zero the “no-load” speed can be computed.

$$\omega_0 = \frac{V_a}{K_e} \text{ rad/sec} \quad (4.6)$$

Since motors often operate over a wide range of torques and speeds, it is difficult to define an appropriate measure of efficiency. The motor constant K_m gives a means of comparing motor efficiency independent of torque and speed.

$$K_m = \frac{T_m}{\sqrt{P_{cu}}} = \frac{K_t i}{\sqrt{I^2 R}} = \frac{K_t}{\sqrt{R}} \quad (4.7)$$

Substituting the motor constant into the torque - speed relationship then gives:

$$T_m = K_m^2 (\omega_0 - \omega) \quad (4.8)$$

This linear torque - speed relationship can be seen in figure 4.1. This is known as a torque-speed curve and has a slope of constant $-K_m^2$ with stall torque $T_s = K_m^2 \omega_0$.

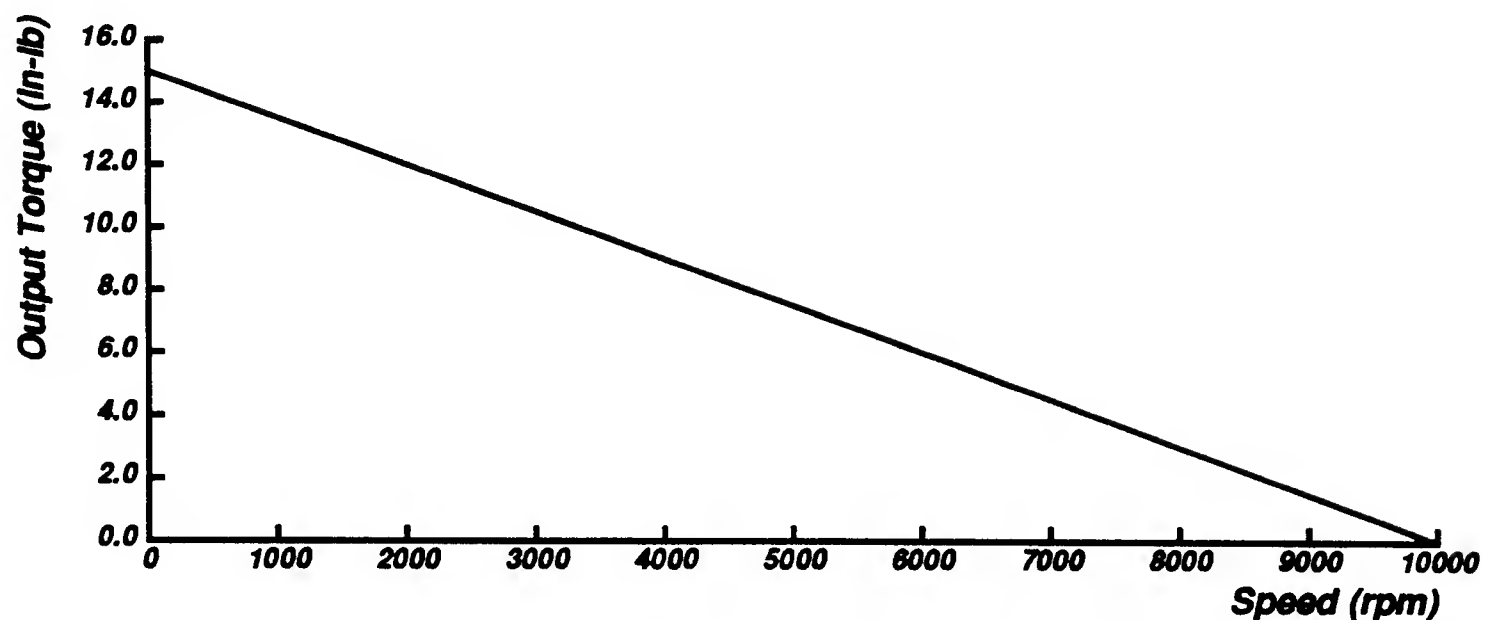


Figure 4.2: Theoretical Torque - Speed Curve.

The resultant power loss due to copper heating is then

$$P_{cu} = I^2 R = \left(\frac{T_m}{K_m} \right)^2 \text{ watts} \quad (4.9)$$

The acceleration of the motor shaft can be estimated by modeling it as a simple inertial load J_m , with bearing friction B_m . This load would then accelerate according to:

$$J_m \frac{d\omega}{dt} + B_m \omega = T_m = K_t i \quad (4.10)$$

Solving for ω above, taking the Laplace transform, and combining with the Laplace transform of 4.1 leaves

$$V_a = (Ls + R)i + \frac{K_e K_t i}{J_m s + B_m} \quad (4.11)$$

The current control amplifier stabilizes the applied motor voltage according to the control law:

$$V_a = K_c(K_v V_c - i) \quad (4.12)$$

where K_c is the gain on the current loop, and K_v is a scale factor relating the actual current to the current command given in volts. Substituting in the term for V_a found in 4.11 gives the transfer function from commanded voltage to current

$$\frac{i(s)}{V_c(s)} = \frac{K_c K_v}{L} \frac{s + \frac{B_m}{J_m}}{s^2 + \left(\frac{B_m}{J_m} + \frac{(R+K_c)}{L}\right)s + \frac{B_m(R+K_v) + K_c K_t}{J_m L}} \quad (4.13)$$

Since $T_m = K_t i$, the open loop transfer function is then

$$G(s) = \frac{T_m}{V_c(s)} = \frac{K_t K_c K_v}{L} \frac{s + \frac{B_m}{J_m}}{s^2 + \left(\frac{B_m}{J_m} + \frac{(R+K_c)}{L}\right)s + \frac{B_m(R+K_v) + K_c K_t}{J_m L}} \quad (4.14)$$

It is evident from this transfer function that the motor is a second order system, with a zero and two poles. The zero will be very close to the imaginary axis since the damping term, $\frac{B_m}{J_m}$, is very small due to bearing friction. The poles are less easily identified. In order to close a tight current loop, the current gain, K_c , is made very large. This causes the system to be overdamped, and drives the poles apart. The high frequency pole moves so far down the real axis that it has little effect on the system. The other pole, however, is driven towards the origin and the system zero. Ideally the pole and zero would coincide and cancel, but the changing damping and inertia in the system cause the zero to move. This pole-zero pair is virtually hidden in a low resolution frequency response of the system, but becomes evident when it dominates the time response.

4.2 Sensor Model

The equations of motion for the motor / sensor pair were derived in chapter 2. Referring to equation 2.2

$$T_s = K_s \theta_s = T_m - (J_h + J_s) \ddot{\theta}_s - B_s \dot{\theta}_s \quad (4.15)$$

There is a proportional relationship between the feedback voltage from the strain gauge amplifier, V_f and the rotation of the sensor shaft:

$$V_f = K_a \theta_s \quad (4.16)$$

The sensor transfer function can then be derived:

$$H(s) = \frac{V_f(s)}{T_m(s)} = \frac{K_a}{(J_h + J_s)(s^2 + \frac{B_s}{J_h + J_s}s + \frac{K_s}{J_h + J_s})} \quad (4.17)$$

Since the sensor is couple directly to the motor stator and housing rather than the rotor, the inertia term, $J_h + J_s$, is the stator and housing inertia, and the damping term, B_s , is the friction between the stator and ground.

This transfer function is a classic second order system. It has two poles at the natural frequency of $\sqrt{\frac{K_s}{J_h + J_s}}$, and a very low damping ratio due to the low bearing friction.

4.3 Controller Model

The controller was relatively simple to implement, due to the system design. Since the PWM motor driver converted a voltage command to torque and the torque sensor transformed torque back into volts, all torque values in the controller were represented

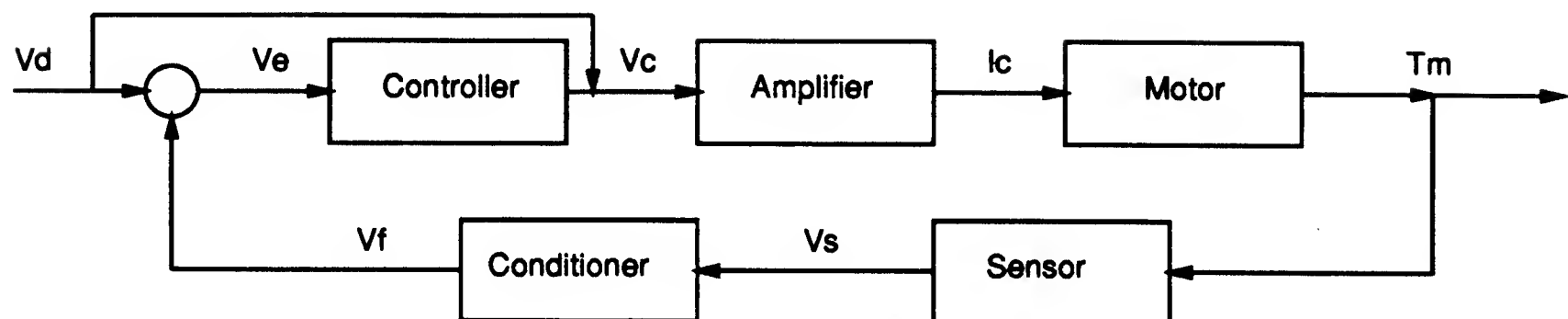


Figure 4.3: High Level Control Block Diagram.

as voltages. The motor amplifier was tuned so that a voltage command of ± 10 volts corresponded to an open loop torque of ± 10 in-lbs. The gains on the strain gauge conditioner were then modified so that a sensed torque of ± 10 in-lbs produced an output of ± 10 volts. This made interfacing and data conversion trivial. A block diagram showing the system components can be seen in figure 4.3.

In this figure, V_d is the desired torque, V_e is the torque error, V_c is the commanded torque from the controller, I_c is the current from the amplifier, T_m is the motor torque, V_s is the sensed torque, and V_f is the torque fed back to the controller.

The standard Proportional + Integral + Derivative controller is:

$$K(s) = \frac{V_c(s)}{V_e(s)} = K_p + \frac{K_i}{s} + K_d s \quad (4.18)$$

with

$$V_e = V_d - V_f \quad (4.19)$$

To increase the response time, the open loop torque command V_d is fed forward through the controller. This allows the controller to simply zero the error between the

open-loop torque and the desired torques, rather than start at the previous torque command and move to the new command.

Combining this with the sensor transfer function, $H(s)$, and the motor transfer function, $G(s)$ yields the closed loop transfer function:

$$C(s) = \frac{T_m(s)}{V_d(s)} = \frac{(K(s) + 1)G(s)}{K(s)G(s)H(s) + 1} \quad (4.20)$$

Notice that the numerator contains a $(K(s) + 1)$ term. For small gains or high frequencies, the system will respond like the open-loop system. The controller then only needs to correct for the errors between open-loop and desired torque. To achieve a faster response, the gain term can be increased, dominating the open-loop response. The higher gain on this controller will make it less stable, possibly resulting in oscillations and limit cycles.

4.4 Bandwidth Estimation

This section will provide estimates of the bandwidth for the motor and sensor. The values used for these computations are the manufacturers' specifications.

Motor Parameters

Model	HHK 0250N013A0A	
Continuous Stall Torque	$T_c = 15$	$in - lb$
Maximum Speed	$\omega_0 = 10,000$	rpm
Torque Constant	$K_t = 2.5$	$in - lb/amp$
Back EMF Constant	$K_e = 30.0$	$V/krpm$
Phase Inductance	$L = 0.93$	mH
Phase Resistance	$R = 2.70$	$ohms$
Rotor Inertia	$J_m = .001125$	$in - lb - sec^2$

from these values were obtained:

Motor Constant	$K_m = 1.52$	$in - lb/\sqrt{watts}$
Electrical Time Constant	$\tau_e = 0.344$	$msecs$
Mechanical Time Constant	$\tau_m = 3.00$	$msecs$

Sensor Parameters

Model	Sensotec QWLC-8M	
Torque Range	$T_{max} = 50.0$	$in - lb$
Deflection at T_{max}	$\phi = 0.25$	$degrees$
Stiffness	$K_s = 11,500$	$in - lb/rad$

Linearity	0.1	percent
-----------	-----	---------

Using the simple motor-sensor model developed in chapter 2 to determine the sensor natural frequency:

$$\omega_n^2 = \frac{K_s}{J_h + J_s} \quad (4.21)$$

The inertia of the motor housing and stator was estimated to be $0.005 \text{ in-lb-sec}^2$, giving a natural frequency prediction of 1516 rad/sec, or about 240 Hz. If the 100 in-lb version of the torque transducer was chosen, the potential bandwidth would be increased to greater than 340 Hz, but would sacrifice torque resolution.

The open loop bandwidth of the motor can be easily calculated from the electrical and mechanical time constants. The formula to determine the motor bandwidth without a current controller is:

$$\omega_n = \frac{1}{2\pi\sqrt{\tau_e\tau_m}} \quad (4.22)$$

Substituting in the motor time constants determined above, the natural frequency of the motor is estimated to about 156 Hz. Since the sensor bandwidth is higher than the motor bandwidth, the addition of the sensor does not degrade performance appreciably. Unfortunately, the bandwidth of the system may be significantly reduced by the controller and amplifier. Related research with the *WAM* motors has shown that the measured controllable motor bandwidth is on the order of 10 Hz, even though the motor bandwidth is greater than 100 Hz. This discrepancy is due to the high current gain inside the motor controller, as described above in the motor model. To achieve a very tight current loop,

the current gain is made very large, which then increases the motor damping and slows the response. Plots showing the dynamic characteristics of the system can be found in chapter 5.

4.5 Torque Ripple

There are many different factors leading to the existence of torque ripple. Stator slots can cause variations in the the air gap reluctance which leads to cogging torque. The saturation of the iron laminations in the magnetic circuit or degradation of the magnetic flux due to temperature dependence of the magnets may also contribute to ripple. A poorly designed or modeled controller may introduce some nonlinearities and higher order harmonics to the system. Offsets and gain differences in the controller often produce a majority of the low order ripple harmonics. PWM amplifiers typically have a deadband which can impose such an offset. Ripple may also occur when there is nonsymmetric demagnetization of the rotor magnets due to armature reaction.

This section will derive and discuss the major contributors of torque ripple for this system. Predictions of these effects will be illustrated. Actual plots of the motor ripple can be seen in chapter 5. To understand the effects of ripple, the standard motor equations derived earlier in this chapter must be modified for this particular system. In a three phase motor such as used in this research, equation 4.4 can be written to include the contribution of each phase to the total current:

$$T_m = K_t [i_a \cos(n\theta) + i_b \cos(n\theta + 120^\circ) + i_c \cos(n\theta - 120^\circ)] \quad (4.23)$$

where n is the number of motor poles and θ is the mechanical angle of the motor shaft. Given the 3-phase wye connection of the stator, i_c is constrained by Kirchoff's current law to be:

$$i_c = -(i_a + i_b) \quad (4.24)$$

Based on the sinusoidal commutation discussed in chapter 2 and seen in figure 2.4, the first order approximation for the current in each phase is:

$$\begin{aligned} i_a &= i \cos(n\theta) \\ i_b &= i \cos(n\theta + 120^\circ) \end{aligned} \quad (4.25)$$

with i_c being determined by the other two phases. The computed theoretical torque for the above constraints is now

$$T_m = \sqrt{\frac{3}{2}} K_t i \quad (4.26)$$

(Notice that this expression differs from the one given in the motor model: $T_m = K_t i$. In that case, and in most motor specifications, the K_t is already scaled by $\sqrt{\frac{3}{2}}$.)

If offset errors and relative waveform magnitudes are included in each phase, the currents become:

$$i_a = A \cos(n\theta) + \delta_a \quad (4.27)$$

$$i_b = B \cos(n\theta + 120^\circ) + \delta_b \quad (4.28)$$

By combining equations 4.23, 4.26, and 4.28 the motor output torque becomes:

$$\begin{aligned} T_m &= \sqrt{\frac{3}{2}} K_t (A \cos^2(n\theta) + B \sin^2(n\theta)) + \frac{1}{2} \sqrt{\frac{3}{2}} K_t (B - A) \sin(2n\theta) \\ &\quad + 2 \sqrt{\frac{3}{2}} K_t (\delta_a \sin(\theta + 120^\circ) - \delta_b \sin(n\theta)) \end{aligned} \quad (4.29)$$

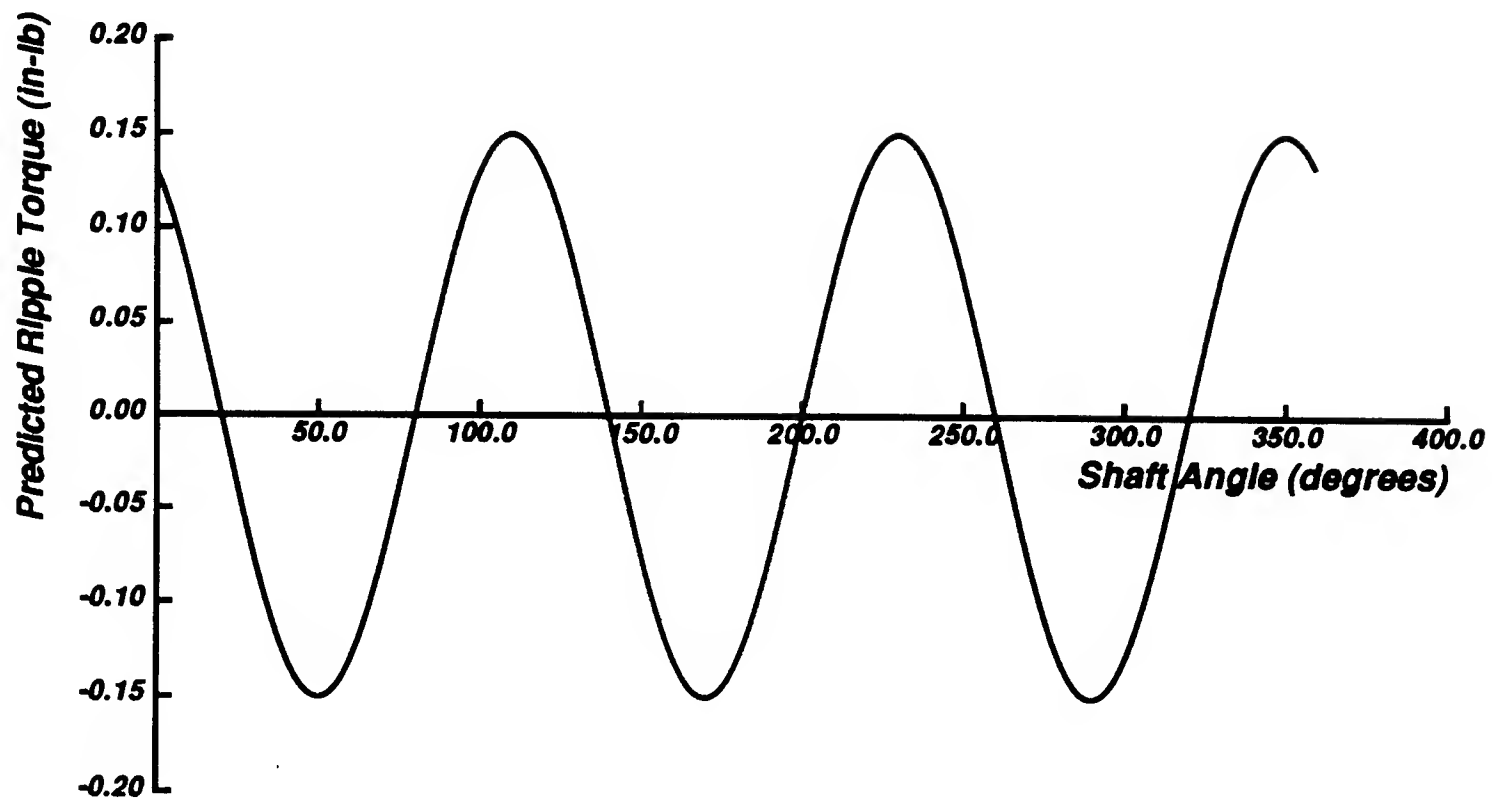


Figure 4.4: First Harmonic for a Three Pole Pair Brushless Motor.

If the two phase current waveform magnitudes, A and B , are equal to a given value of i , and $\delta_a = \delta_b = 0$, the output torque reduces to the equation given in 4.26. However, if $A = B = i$, but $\delta_a \neq 0$, the resulting equation is

$$T_m = \sqrt{\frac{3}{2}} K_t i + \frac{1}{2} \sqrt{\frac{3}{2}} \delta_a K_t \sin(n\theta + 120^\circ) \quad (4.30)$$

This clearly shows that an offset in one of the phases will cause a ripple at the fundamental frequency of $n\theta$. This ripple is independent of torque and should remain constant for the full range of torques. Figure 4.5 shows a prediction of the first harmonic for a brushless motor with three magnet pole pairs ($n = 3$).

Another major cause of ripple can be seen by assuming the waveform magnitudes are unequal, $A = B + \Delta_a$, with $\delta_a = \delta_b = 0$. Equation 4.29 then takes the form

$$T_m = \sqrt{\frac{3}{2}}K_t B + \sqrt{\frac{3}{2}}K_t \Delta_a \cos^2(n\theta) - \frac{1}{2}\sqrt{\frac{3}{2}}K_t \Delta_a \sin(2n\theta) \quad (4.31)$$

Using the identity $\cos^2\theta = \frac{1}{2} + \frac{1}{2}\cos 2\theta$

$$T_m = \sqrt{\frac{3}{2}}K_t(B + \frac{\Delta_a}{2}) + \sqrt{\frac{3}{2}}K_t \Delta_a \cos(2n\theta + 30^\circ) \quad (4.32)$$

This equation demonstrates that a difference in the current waveform magnitude of two phases of the motor can generate torque ripple at twice the fundamental driving frequency of $n\theta$. The magnitude of this ripple harmonic would be approximately $\sqrt{\frac{3}{2}}$ times the phase gain error. Since this error is in the phase gain, it will scale with the commanded torque. Additionally, the DC component of the torque will be the average of the two phase gains, as seen in the first term of 4.32. Figure 4.5 shows the estimated second harmonic component of ripple at torque commands of 1.0 and 5.0 in-lb.

Several other factors can influence torque ripple, although much less significantly than the first two harmonics. A current loop deadband in the controller can cause a limit cycle, which then manifests itself as torque ripple. Unmodeled spacial harmonics in the motor may also cause ripple unless compensated by higher order waveforms superimposed on the commutation waveform. Indepth analysis of these and other causes of ripple can be found in several references. Paul [Paul 87] modeled the first two harmonics for Moog brushless motors, and fed forward the appropriate currents to cancel some of the ripple effect. He was able to reduce the torque ripple by as much as 50%. LeHuy, Perret, and Feuillet [Le-Huy 86] modeled the spacial harmonics of a three phase disk-type motor by monitoring the back EMF in the phase windings. They then modified the commutation

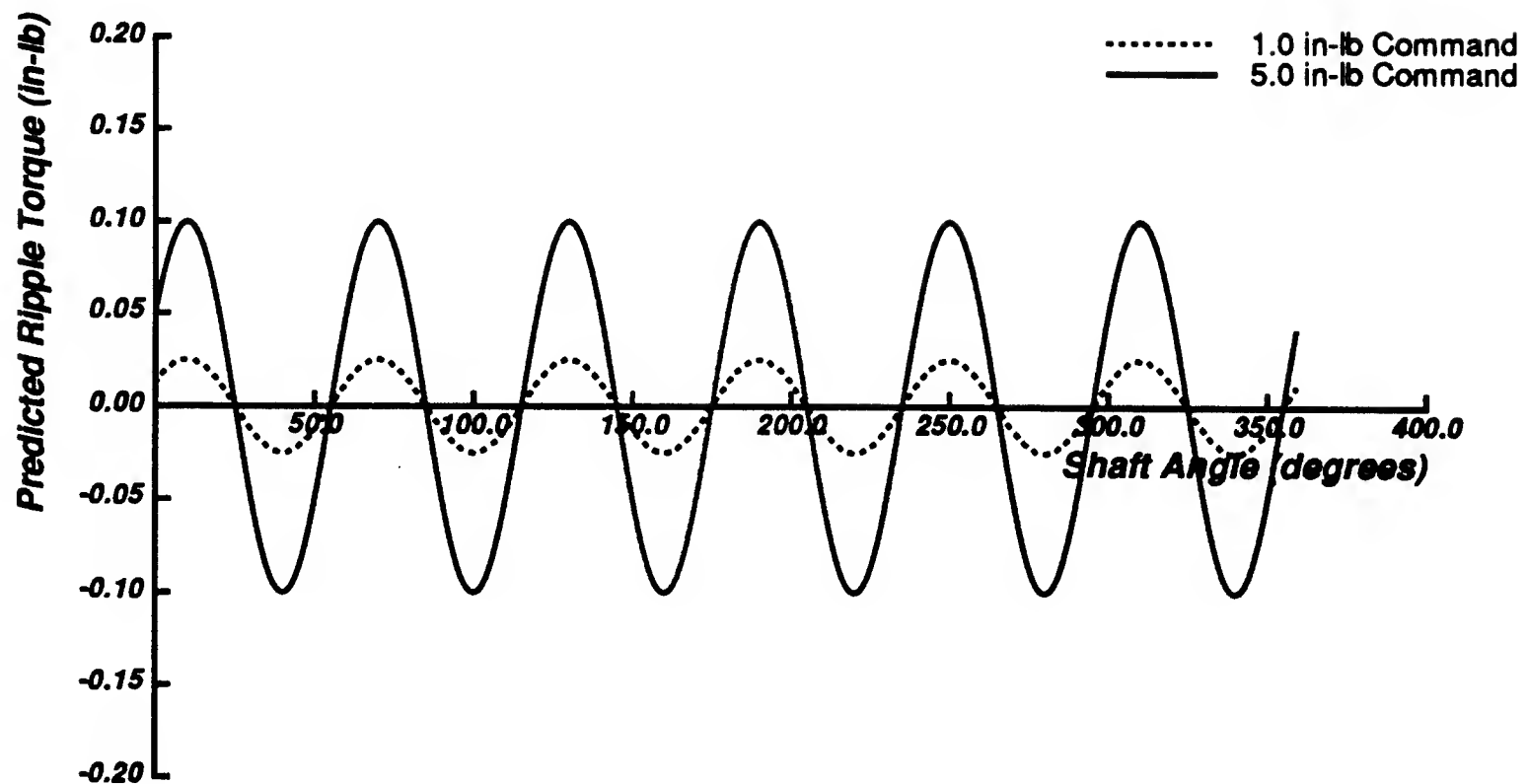


Figure 4.5: Second Harmonic for a Three Pole Pair Brushless Motor.

waveforms to reduce the low frequency harmonic ripple by 70%.

4.6 Friction Models

There is a measurable amount of friction in the actuator system. It takes the form of Coulomb friction, stiction, and viscous damping. While it is possible to linearize viscous damping as a function of velocity, both Coulomb friction and stiction are discontinuous at zero velocity. These non-linear properties may cause limit cycling and other unpredictable behavior in the regions where they are discontinuous.

These three models of friction can be seen in figure 4.6. In the Coulomb friction model the friction torque is constant for all velocities except zero, where it switches sign. This essentially causes a deadband that is the magnitude of the friction. Many controllers

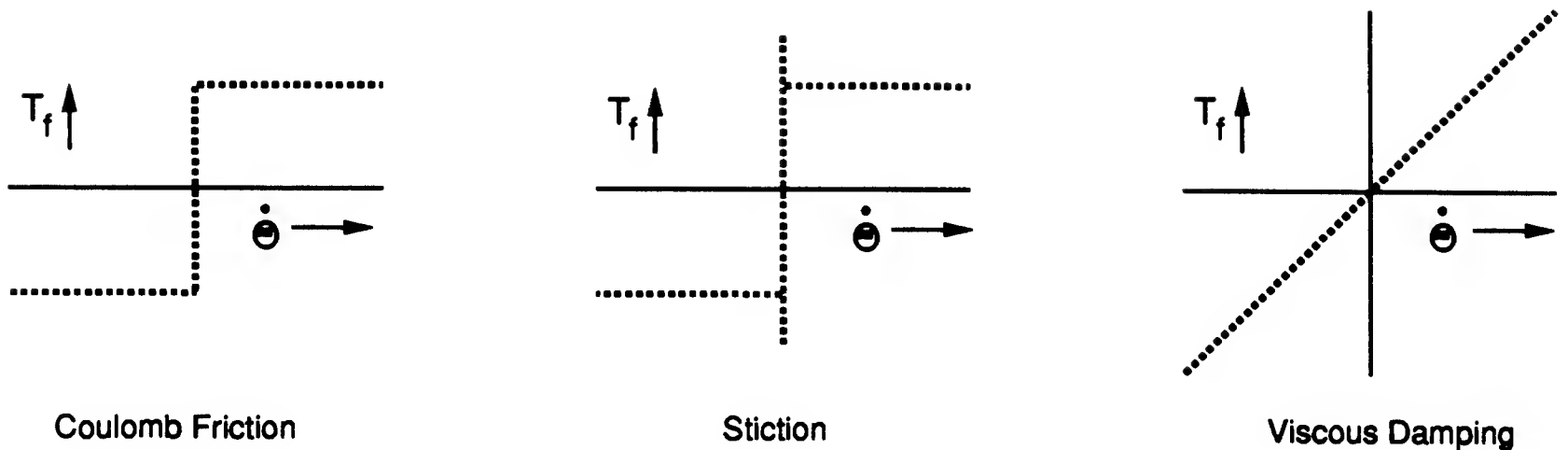


Figure 4.6: Common Models of Friction.

utilize a feedforward compensation technique to minimize the effect of Coulomb friction.

Stiction compounds this problem by adding a higher breakaway torque to the constant Coulomb friction. This makes it virtually impossible to control small velocities since the controller has to overcome the stiction without overshooting the target torque. Feedforward techniques are not as accurate as those for Coulomb friction, as the controller needs to switch between the modeled stiction value and the Coulomb value.

Linear friction, on the other hand, is fairly simple to model. A first order approximation of the friction as a function of velocity is usually adequate for most applications. Unfortunately, linear damping rarely occurs without one of the other friction types. The bearings supporting the motor shaft, for example, exhibit stiction like behavior at zero velocity, but change to linear damping for all other velocities.

In open-loop force control applications the various forms of friction can seriously corrupt the output torque. The Coulomb friction and stiction not only act as a deadband, but subtract directly from the output torque. The linear damping causes a disturbance

in torque that varies proportionally with speed. All of these forces have the effect of reducing the actual torque to below the command.

A properly designed closed-loop torque controller should be able to compensate for all of these effects with the possible exception of stiction. Since the error induced by Coloumb friction is constant, an integral controller is required to drive the error to zero. The same is true for the linear damping, provided that the rate of change in motor speed is not greater than the integral gain. This method will not always work when stiction is present. The controller may constantly overshoot the stiction level in one direction, and then overcompensate in the other. This would cause a stable limit cycle about the stiction value. If the sensor and actuator were fast enough, it is possible to break out of this limit cycle and minimize the torque error.

Chapter 5

Results

This chapter will discuss the performance of the actuator under both open and closed loop control. Data plots are included to illustrate the effects of friction and ripple.

5.1 Open Loop Actuator Characteristics

This section includes the baseline characteristics of the actuator system. Before proceeding to the open loop control accuracy, we will first discuss the methods used to determine the friction in the system, and how to accurately calibrate the sensor.

5.1.1 Bearing Friction

As discussed in the previous chapter, there is a measurable amount of bearing friction in the actuator system. This friction can best be seen by a comparison of the clockwise and counterclockwise torques measured with the motor disabled, as seen in figure 5.1. The offset between the two curves is approximately 0.13 in-lb and stays relatively constant. This deadband between the two curves is a characteristic of stiction and Coulomb friction.

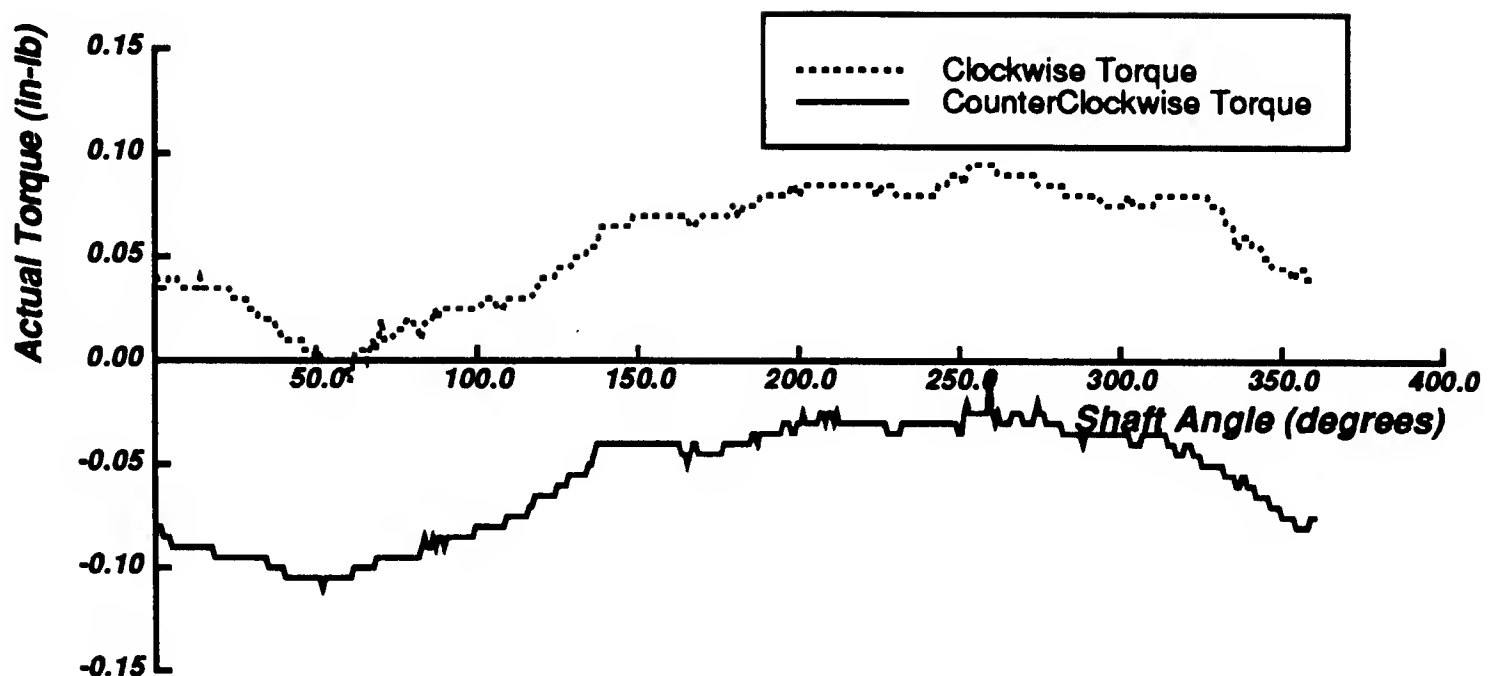


Figure 5.1: Clockwise and Counter Clockwise Torque with Motor Disabled.

Since these measurements were taken at a constant, non-zero velocity, this offset must be due to Coulomb friction. In roller bearings, Coulomb friction should be equal in both directions, therefore it is half of this deadband value, or ± 0.065 in-lb.

5.1.2 Sensor Calibration

The bearing friction described above makes it very difficult to calibrate the zero point of the torque sensor. In order to minimize the offset error, the motor is commanded to exert an open loop torque of 0.1 in-lb in the clockwise direction. Several torque samples are taken after the system has reached this steady state torque. The torque command is then set to 0.0, the motor disabled, and more samples are taken. The same procedure is then repeated for torques of -0.1 in-lb and 0.0 again. Each of the 0.0 in-lb tests is averaged individually and then together to determine the offset. The ± 0.1 in-lb samples are used to determine if the gain calibration of the sensor agrees with the amplifier gain.

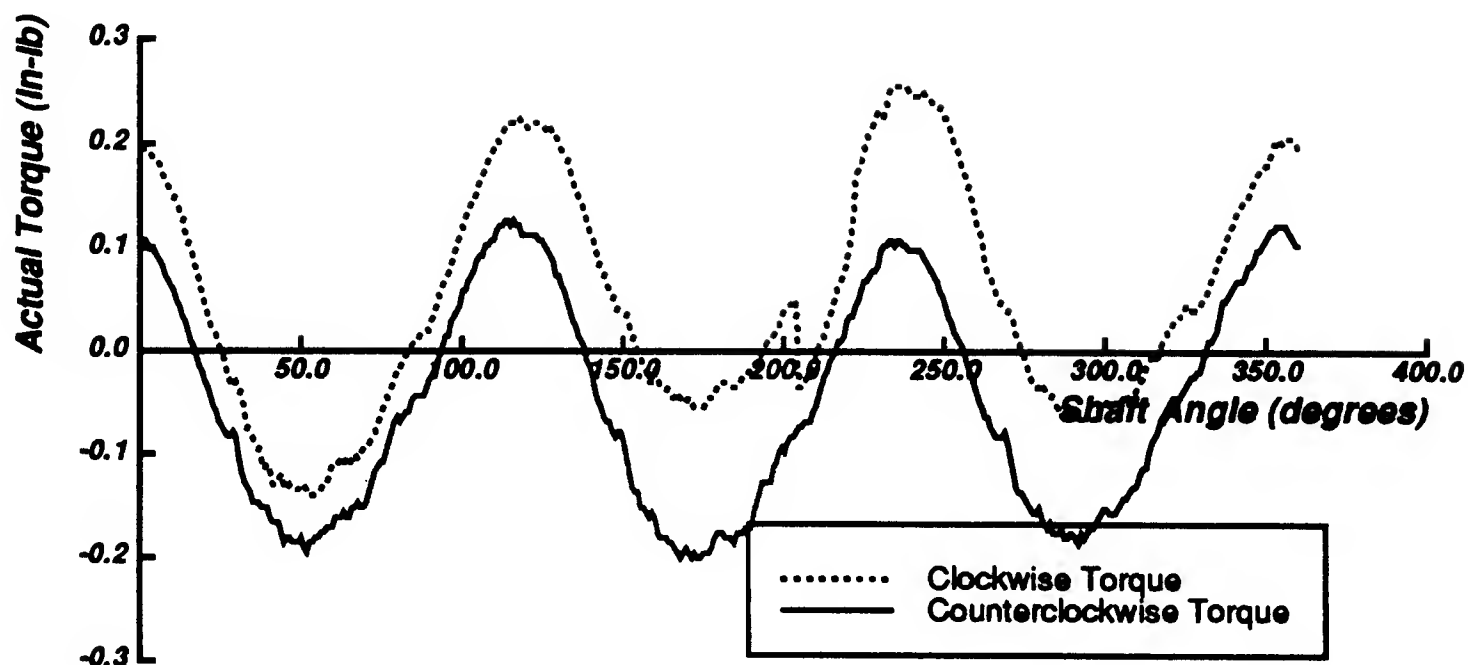


Figure 5.2: Effect of Ripple on CW and CCW Rotation.

5.1.3 Torque Ripple

The effect of torque ripple can be seen very clearly in figures 5.2 and 5.3. Figure 5.2 shows the ripple with a 0 in-lb commanded torque. The motor shaft was rotated by hand in both the clockwise and counterclockwise directions. The first order harmonic of 3 cycles per revolution is plainly visible. It has a peak to peak magnitude of about 0.3 in-lb, and remains for all values of torque. The offset between the two curves is due to the bearing friction as mentioned above.

Figure 5.3 shows the second order harmonic torque ripple. This was found by subtracting the first order harmonic ripple in figure 5.2 from the actual torque generated with an open loop torque command of 5.0 in-lb. The effect of this 6 cycles/rotation waveform can be seen by the way the peaks of the open loop torque plot are alternately truncated and expanded. The open loop torque is no longer the smooth sine wave it was

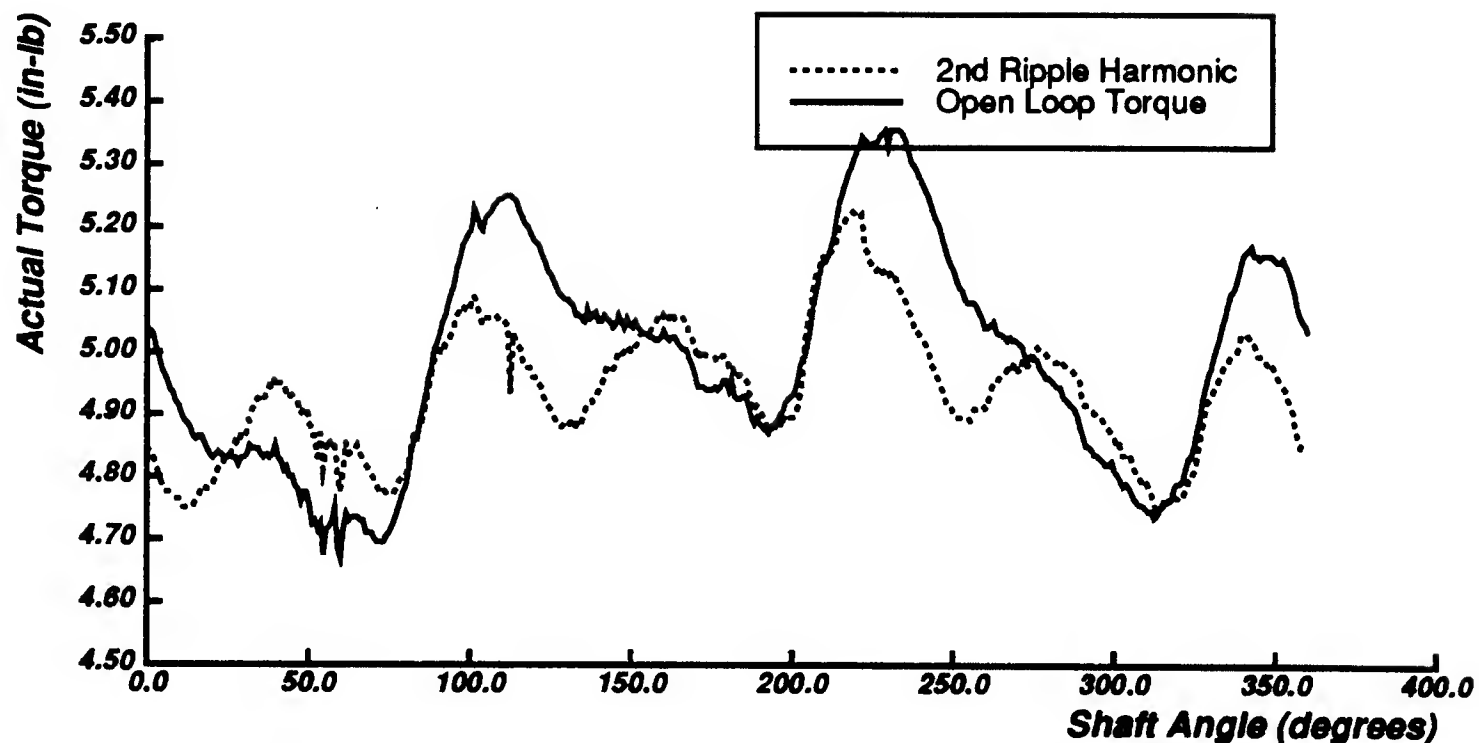


Figure 5.3: Open Loop Torque and 2nd Ripple Harmonic.

at zero command.

5.2 Open vs Closed-Loop Performance

The quasi-static torque accuracy of the actuator was measured by commanding a torque and then rotating the shaft through one complete revolution by hand. The duration of rotation was approximately 1 second. Tests were performed in both directions of rotation to determine the effects of friction.

The compensation for the closed-loop testing consisted of a standard PID controller with unity feedforward of the open-loop command. Several different gains were studied. The system was very robust for low gains. A simple integrator was the only compensation required to eliminate the steady state error. Various proportional and derivative gains were implemented to determine their effect on response time and settling. A high pro-

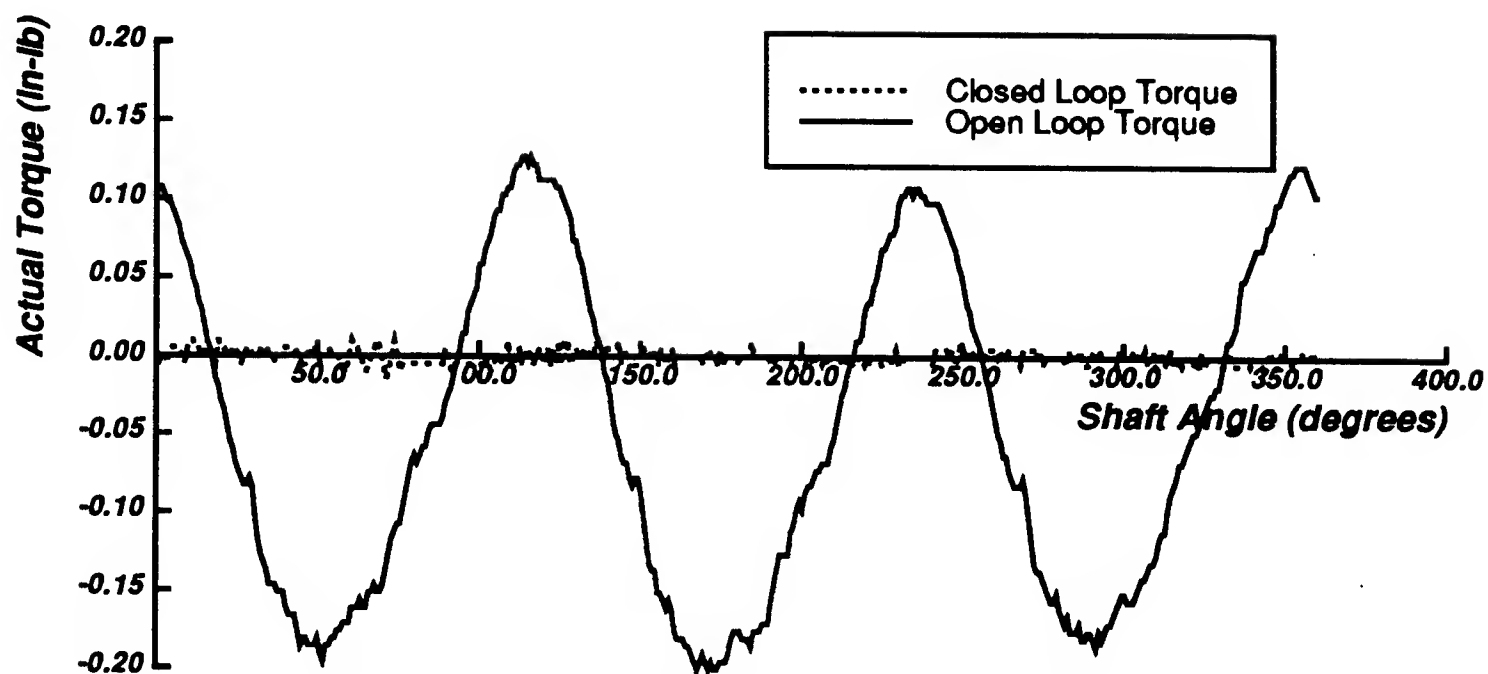


Figure 5.4: Open and Closed Loop Torque at 0 in-lb Command.

portional gain with very low derivative and integral gains produced the fastest response, yet was stable with high accuracy under all conditions.

A plot of the closed loop 0.0 in-lb torque has been superimposed on the corresponding open loop torque in figure 5.4. The open loop torque shows errors of up to 0.2 in-lb due to ripple. The closed loop torque, on the other hand, is accurate to within 0.01 in-lb, which is the noise level of the data acquisition system. This shows an improvement by a factor of 20 by closing the feedback loop.

Figure 5.5 shows the effect of static friction on open loop torque, and the negation of this disturbance by the feedback controller. Notice that the two open loop curves are offset by approximately 0.13 in-lb, the value calculated above in section 5.1.1. Errors in the open loop case reach as high as 0.38 in-lb, while the closed loop torque is always within 0.01 in-lb of the set point.

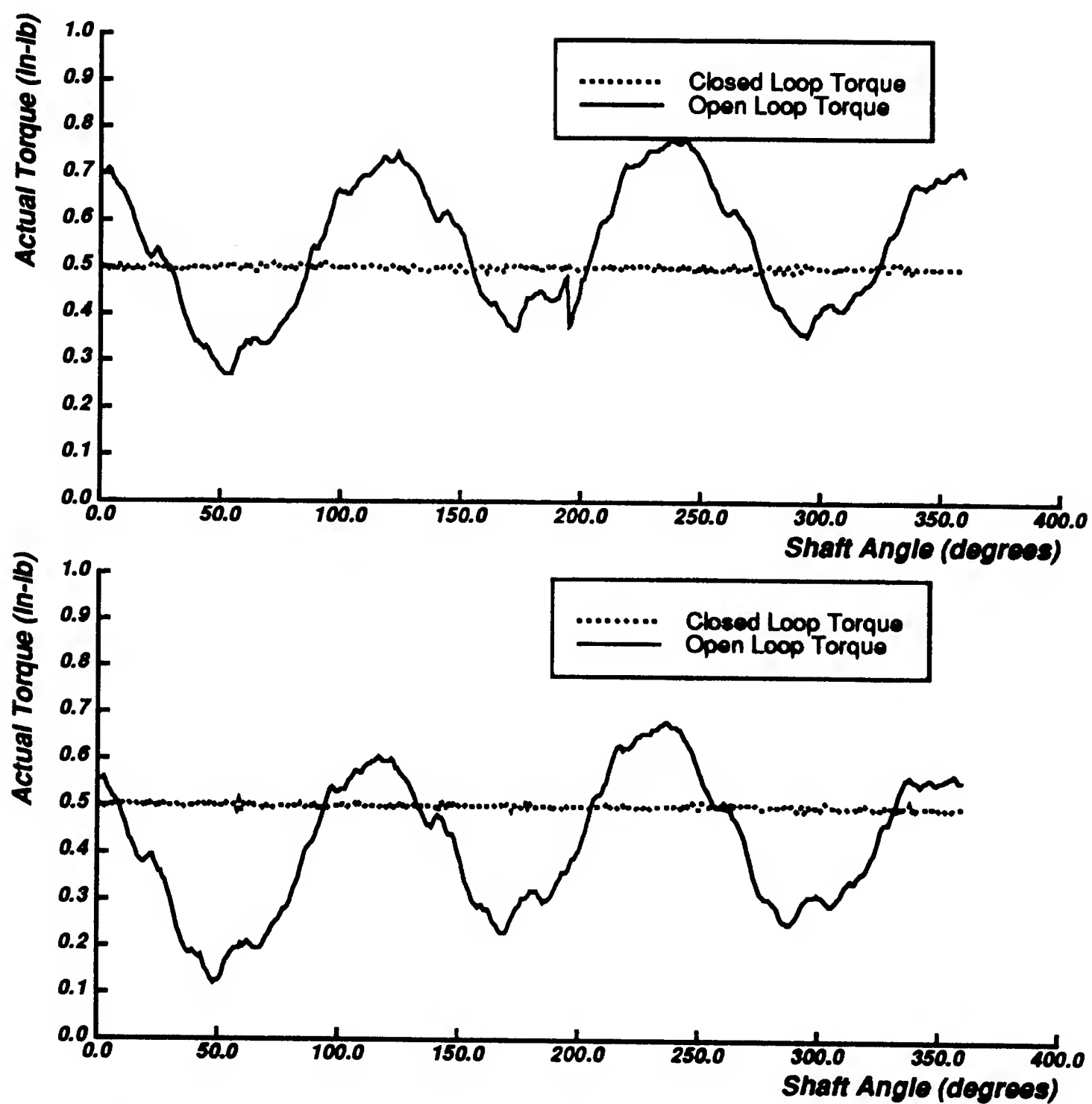


Figure 5.5: Open Loop Torque in Both Directions at 0.5 in-lb Command.

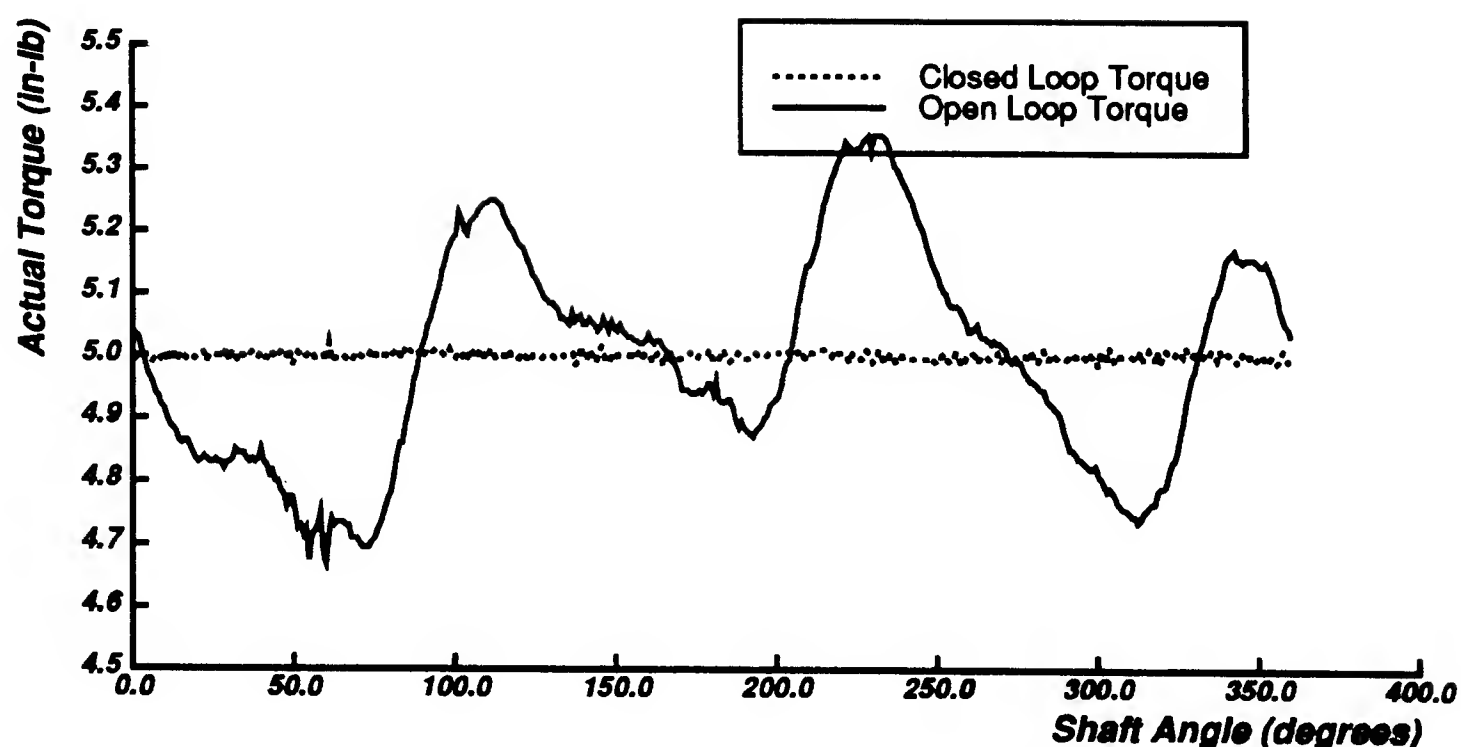


Figure 5.6: Open and Closed Loop Torque at 5.0 in-lb Command.

Figure 5.6 shows the open and closed loop torque for a command of 5.0 in-lb. The closed loop torque has been enlarged as figure 5.7 to show that the peak deviation from command is only 0.02 in-lb. Since this accuracy is virtually independent of torque, it will remain near this level for all commands up to peak torque. This value corresponds to an accuracy of 0.13% over the continuous torque range, giving a dynamic range of 750:1. If we disregard only 10 of the 4000 data points, the error is halved to 0.07%, and the dynamic range doubles to 1500:1. Either value is an order of magnitude better than the open loop error of more than 0.35 in-lb., or 2.3%. By comparison, the Moog 303-003 motors currently being used in the WAM are accurate to about 1.0 in-lb at full torque, or 6.6%.

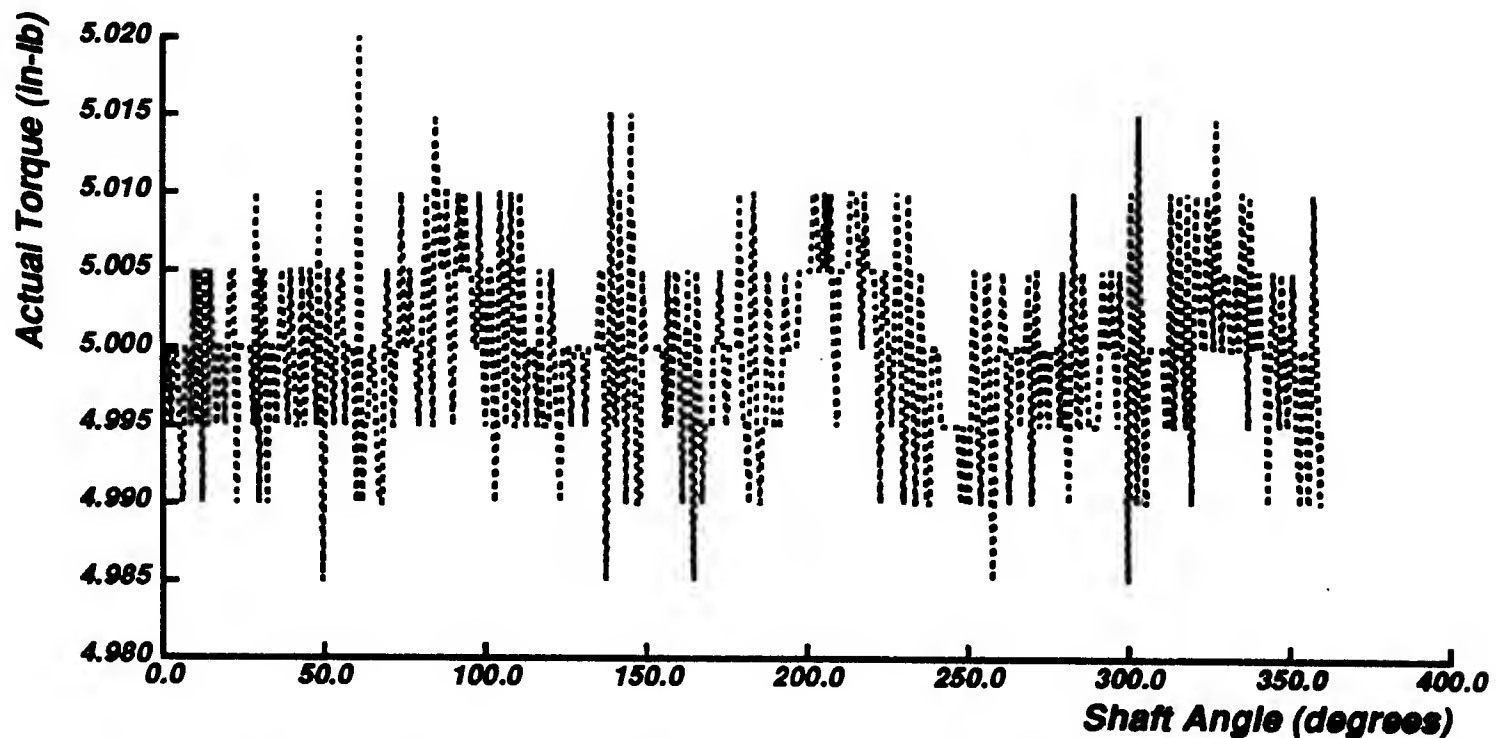


Figure 5.7: Magnification of Closed Loop Torque at 5.0 in-lb Command.

5.3 Dynamic Response

The frequency response of the actuator system was measured using a Hewlett-Packard spectrum analyzer. The unit contained a signal generator which produced a white noise input to the system. The output torque was fed back into the analyzer, and a Fast Fourier Transform was performed between the input and output torque. The resulting magnitude and phase plots for the open loop system can be seen in figure 5.8. As can be seen from these plots, the response is perfectly flat at 0 dB until about 200 Hz where it starts to rise. At approximately 300 Hz, the response peaks to about 20 dB, and then falls off rapidly. This response is characteristic of a second order system with a natural frequency of 300 Hz. The rise is caused by the excitation of the resonant mode, with a 40 dB/decade roll off due to the double pole. The phase slowly shifts until it crosses 90°

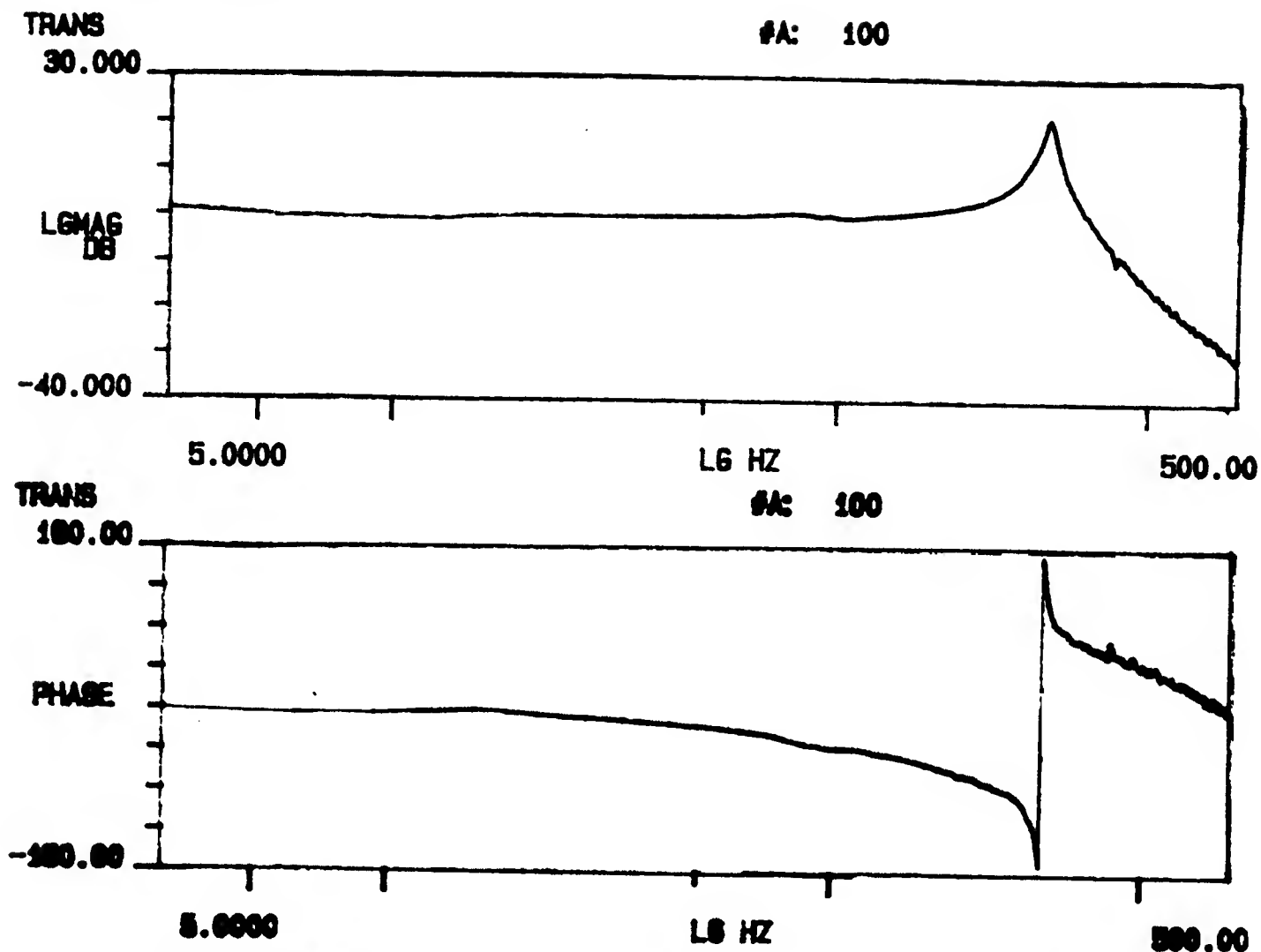


Figure 5.8: Frequency Response of the Open Loop System.

at about 275 Hz. It then falls off steeply and until it crosses 180° very close to 300 Hz. This test was repeated under several different conditions: with the rotor freely rotating, lightly damped, and rigidly fixed. The frequency response for all situations was identical, showing that the stator and rotor are completely decoupled, as predicted by the sensor model.

The response in figure 5.8 plainly shows the double pole at the motor-sensor resonant frequency. However, it does not show the low frequency pole-zero pair predicted by the motor model. To achieve better resolution at low frequencies additional testing was performed with the analyzer bandwidth reduced to 12 Hz. This higher resolution, as

seen in figure 5.9, shows the magnitude dropping to -4 dB at very low frequencies, rising slightly at about 4 Hz, and then leveling out to 0 dB at 7 Hz. This shows that the zero and pole do exist, at 4 and 7 Hz, respectively. On a similar test, conducted with a lower magnitude white noise, the results were significantly different. The zero and pole appear to have shift right, to approximately 5 and 9 Hz, respectively. The magnitude now ranges from -10 to +5 dB. Since the amplitude of noise exciting the system is the only difference in these tests, this change must be due to a nonlinearity. One possible cause is the friction in the bearings. For high noise amplitudes, the bearings exhibit viscous damping, but fall into the Coulomb friction range for low amplitudes. The effect of Coulomb friction and stiction would tend to move the pole and zero further away from the imaginary axis. A frequency response plot of this phenomena can be seen in figure 5.10.

Similar frequency response analysis was performed on the system through the controller. With the controller commanding an open loop torque, the response was virtually identical to that found for the system without the controller. The magnitude peaked at the same 300 Hz frequency, but the phase was slightly shifted. This phase shift corresponded to

$$\phi = 2\pi f t_d \quad (5.1)$$

where f is the frequency and t_d is the delay time associated with the digital sampling and loop execution speed. For this system, $t_d = 0.001$ seconds. At lower frequencies this shift was not significant, but at frequencies near 500 Hz the shift was 180° .

While the low frequency pole and zero are not readily apparent in the frequency

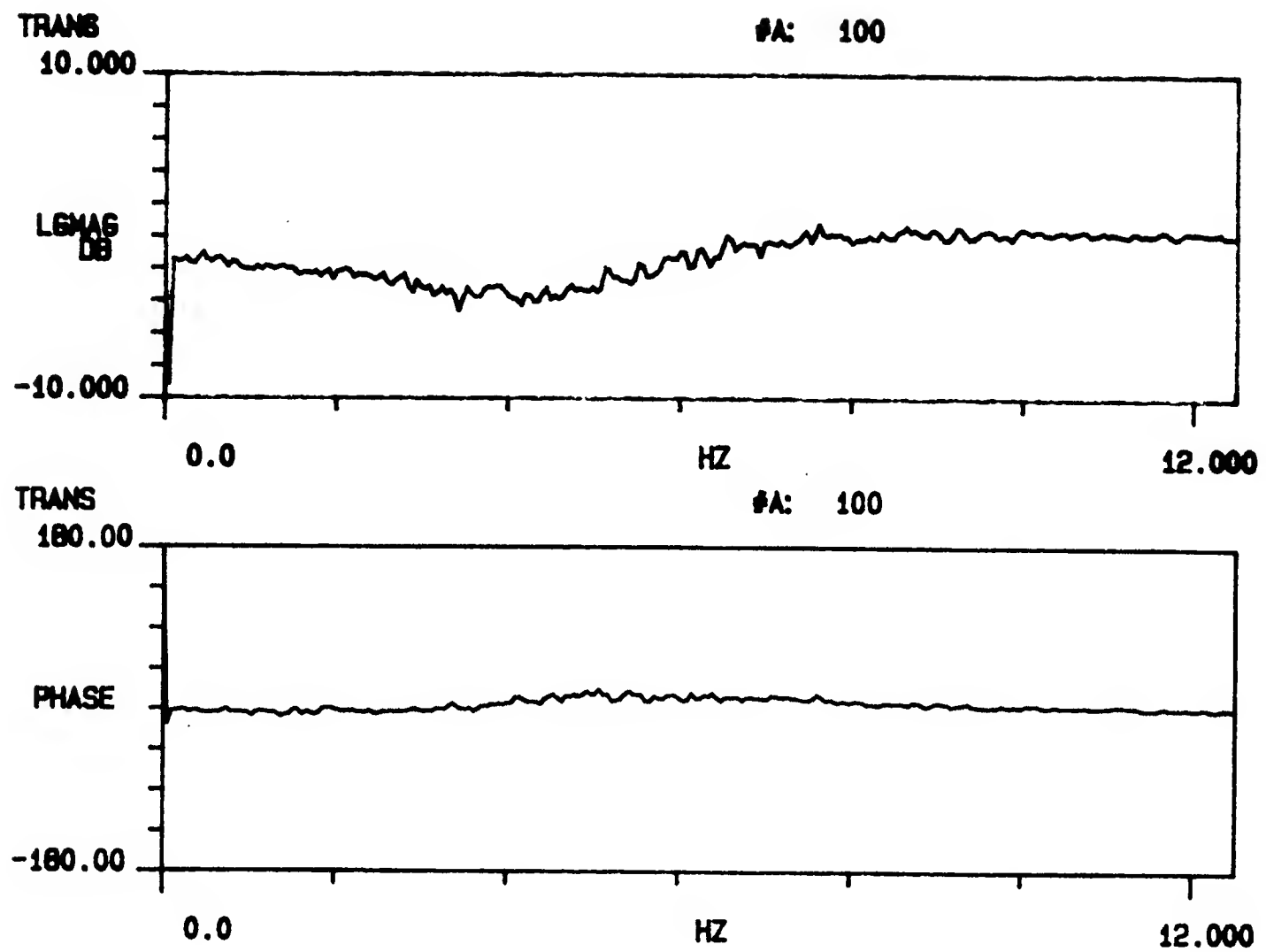


Figure 5.9: Response of the Open Loop System at Low Frequencies.

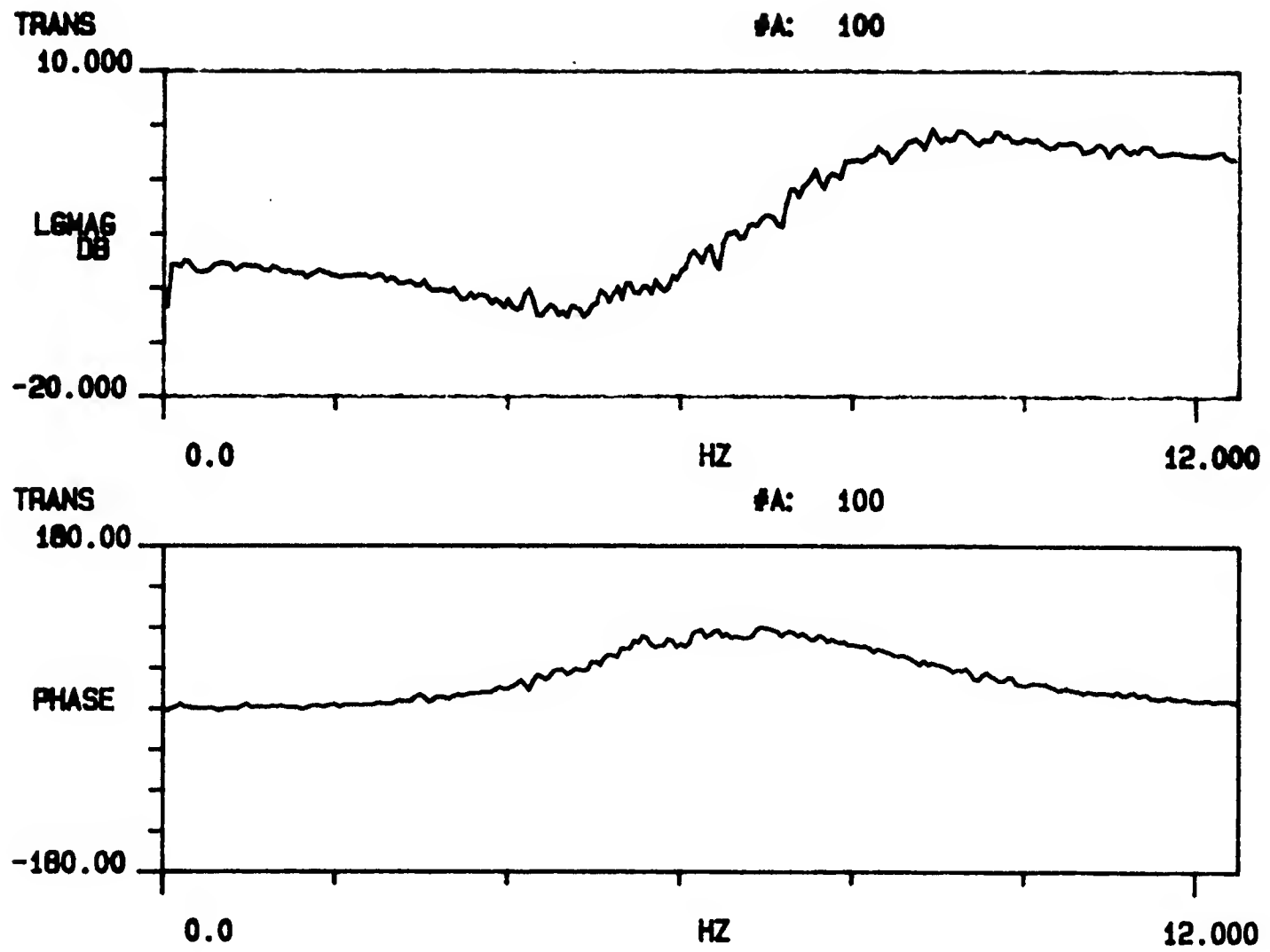


Figure 5.10: Low Frequency Response with Small Amplitude Excitation.

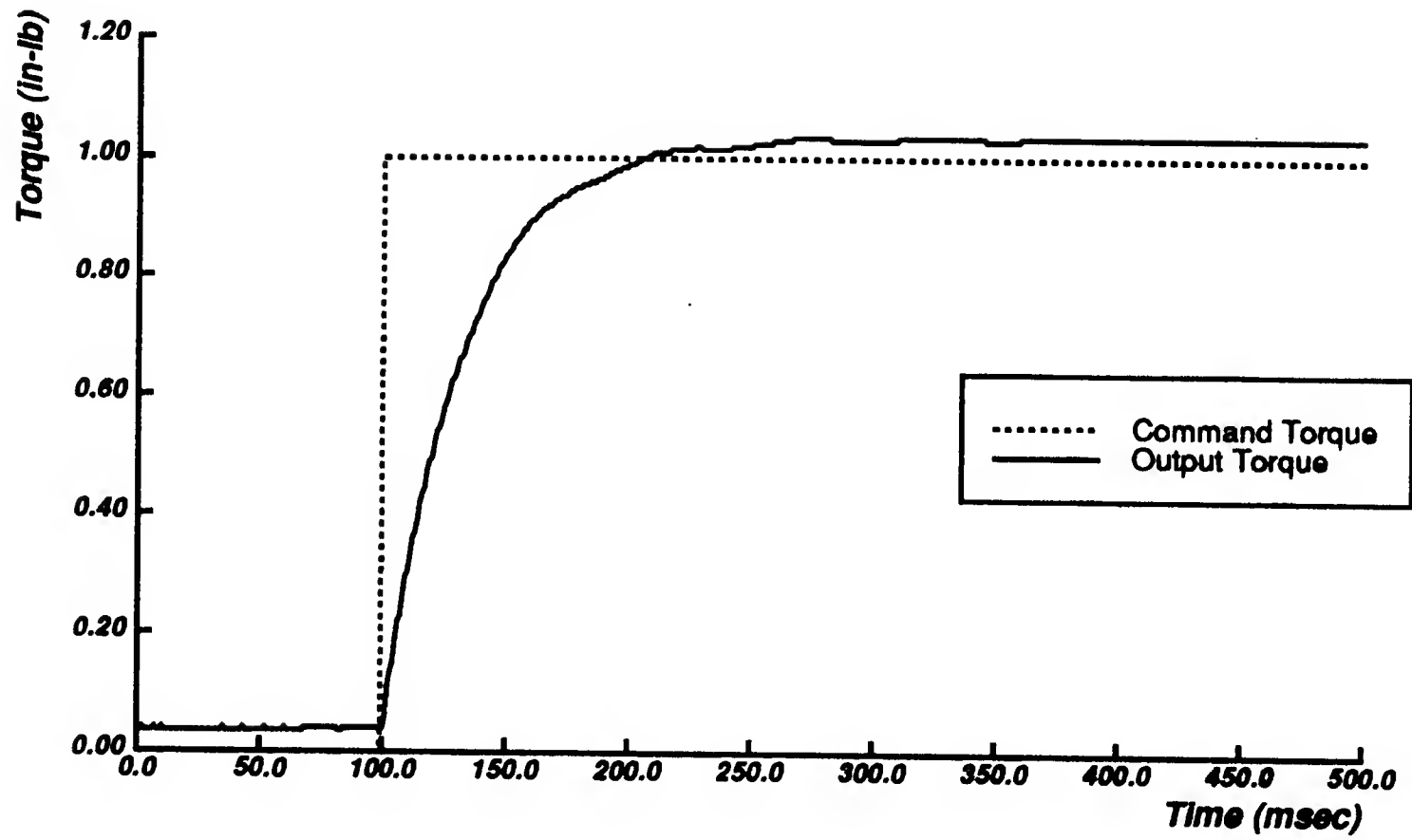


Figure 5.11: Step Response of the Open Loop System.

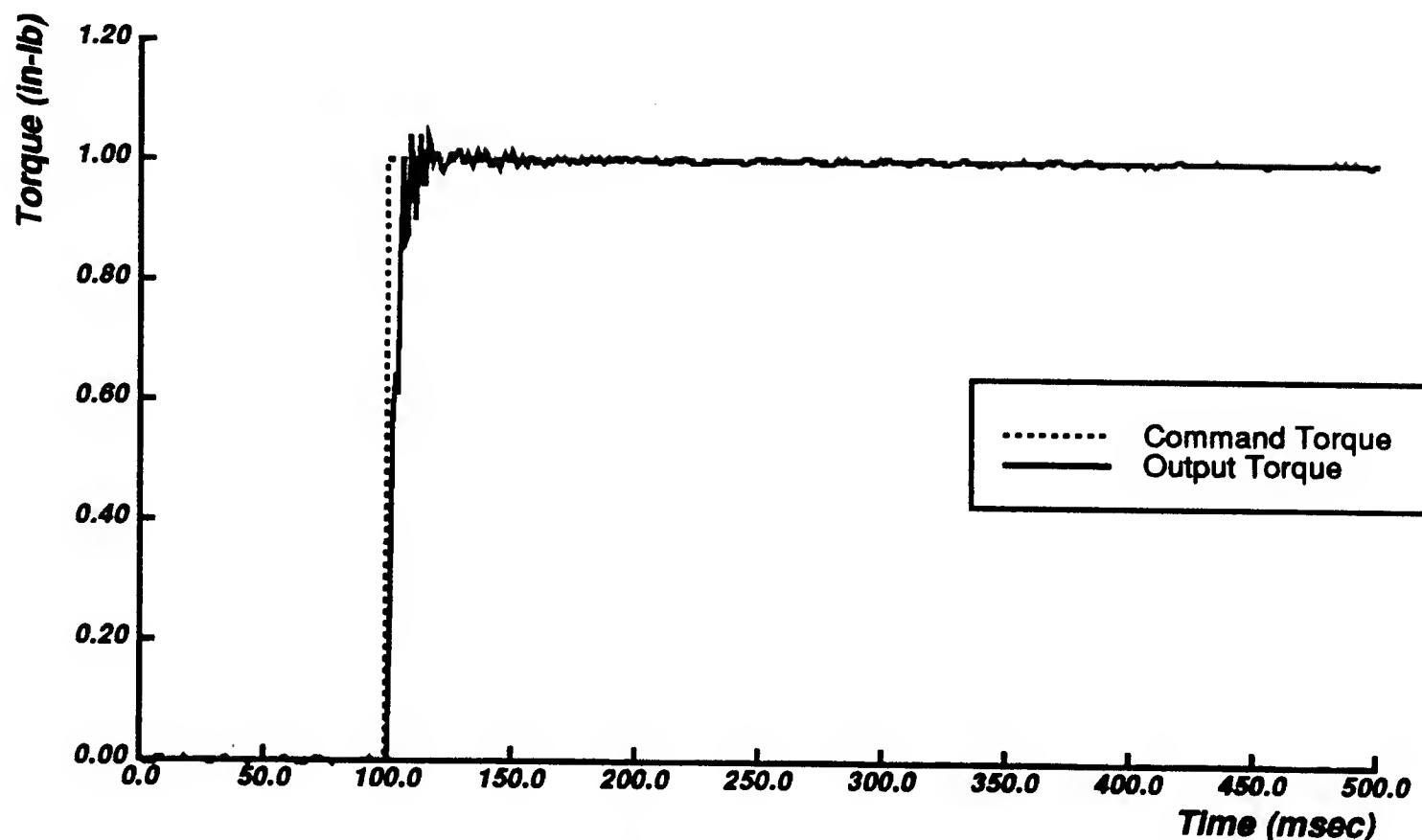


Figure 5.12: Step Response with PID Compensation.

response, they are very obvious in a time response. Figure 5.11 shows the response of the actuator subjected to a step torque input of 1.0 in-lb. The rise time of this overdamped response is 105 msec, approximately what could be expected from a system with a pole between 7 and 9 Hz. The steady state error in this system is 0.035 in-lb.

Although the low frequency pole introduced by the current controller severely damps the open loop response, it is possible to speed the system up with the appropriate compensation. The frequency response of figure 5.8 shows that there is a substantial phase margin up to about 200 Hz. It should therefore be possible to increase the response significantly without instability.

The addition of a high gain PID controller speeded up the rise time by a factor of

20 or more (figure 5.12). For one set of gains, the system crossed the command torque in 5 msec, and settled to within 5% in 11 msec and 2% in 20 msec. In tests with another compensator the rise time was as little as 3 msec, but the system required 16 msec to settle. Using the rise time as a benchmark, bandwidths of 200 - 300 Hz can be inferred. For different applications, the PID gains should be chosen to meet the particular response or settling requirements of the system.

These time responses could probably be improved by closing a faster servo loop. Since this controller was running at only 1 kHz, each oscillation corresponded to 1 or 2 data points, and the entire rise time was as little as 3 samples. For bandwidths approaching 200-300 Hz, the controller should have a servo rate of more than 3 kHz.

Chapter 6

Conclusion

6.1 Summary

As the field of robotics expands, more emphasis is being placed on manipulators capable of operation in unstructured environments. A new field, *Whole Arm Manipulation*, has been developed to address some of the problems associated with unstructured environments. A *Whole Arm Manipulator* is capable of grasping and moving objects with its links in addition to using an end-effector. Since the workspace is no longer constrained to be at the end-effector, the manipulator must be able to identify and control forces anywhere along its links. Rather than instrument the entire arm with sensors, a method was developed to infer contact forces and locations from joint torques. Since this solution may be poorly conditioned in some configurations, accurate torque control and measurement is critical to the force control and collision detection of the *WAM*.

A closed loop torque controlled actuator was developed to provide smooth, accurate torques and minimize the errors associated with ripple, friction, and other disturbances. The actuator uses a reaction torque sensor to measure the actual torque exerted by the

motor. A proportional + integral + derivative controller was implemented to minimize the torque error and decrease the response time.

This thesis studied the issues involved in designing an actuator for torque control. Motor and sensor characteristics for accurate torque control were discussed in detail. A permanent magnet brushless motor was selected for its high torque output, low friction, and reliable operation. The reaction torque sensor was chosen over the inline and joint mounted sensors to decouple the transmission dynamics from the feedback loop. This enabled the system to obtain a much higher bandwidth than the manipulator dynamics would have allowed.

Each of the major components of the actuator was modeled to predict the overall system response. Additional modeling was performed to analyze the nonlinear effects of torque ripple and the various types of friction.

Open and closed loop tests were conducted to compare the accuracy of the sensor and controller. Open loop errors were found to be as large as 0.35 in-lb for a 5.0 in-lb command, or 7%. These errors are primarily due to torque ripple and offset caused by Coulomb friction in the bearings. The closed loop system is capable of controlling torque accuracy to within 0.01 in-lb over a ± 15 in-lb range, for less than 0.1% error. The dynamic range provided by this system is on the order of 1500:1, with the accuracy limited by the quantization noise of the sensor and electronics.

The sensor bandwidth was found to be approximately 300 Hz, which was slightly higher than estimated and three times larger than required. The frequency response analysis showed that the system behaved as a textbook second order system. However,

there was a hidden pole-zero pair at very low frequencies due to the current control scheme utilized in the drive electronics. This limited the open-loop bandwidth to less than 10 Hz, with a corresponding rise time of about 105 msec for a step response. A PID compensator has been shown to speed up the response to 3 msec, predicting a controllable bandwidth of up to 300 Hz. This demonstrates that it is possible to drastically improve the response of a motor by closing a high bandwidth torque loop.

6.2 Problem Areas

The greatest problem in the design and implementation of this system was in reducing the electromagnetic noise produced by the motor controller. This noise consisted of voltage spikes up to 10 volts peak to peak, and were generated at the PWM switching frequency of 16 kHz. This noise circulated throughout the laboratory and could be picked up by the oscilloscope as far as 20 feet away. The computer cage and rack acted as a large antenna, putting the noise back into the torque and position signals that had been so carefully amplified and filtered. All of the cables had to be double shielded and tied to a common ground. Bypass capacitors were liberally used to filter the noise out of signal and power lines. Eventually most of the noise was filtered out by all of the hardware precautions in conjunction with a software low pass filter.

One of the worst problems encountered in a design project such as this is receiving custom made parts in a timely manner and to specifications. Both the motor and sensor were several weeks late and had major differences from the original design. This necessitated a complete redesign of the actuator housings to accomodate the deviations.

Other minor problems included motor - driver compatibility and resolver phasing. The motor and resolver were sent to Infranor so that the amplifier could be properly tuned to the motor characteristics and phased correctly. This caused a delay of three weeks in the implementation.

6.3 Future Research

The intent of this research was to develop a method and hardware to provide a very high accuracy torque source for the *MIT WAM*. It is expected that this prototype actuator will be installed on the *WAM* in the very near future. If the implementation of this first system proves to be successful in improving the force accuracy and position detection of the manipulator, additional actuators would be installed for the other three joints. The computational power required to control all of these actuators would then be significantly greater than that currently provided by the Condor development system. Individual controller boxes would need to be designed to perform all data collection and control for each motor. These modules would be able to receive a torque command from the supervisory computer, read the actual torque put out by the motor, and close the torque loop. It would also return motor information such as position, velocity, and temperature to the host. This would alleviate the Condor system or other high level controller of the computational burden of filtering the position and velocity data and closing the servo loop.

Another improvement in this system would be the development of a scheme to feed-forward some of the ripple and friction terms. This would decrease the required control

effort and improve the accuracy of the system for higher rotational velocities. A very fast observer or estimator model would also increase the response speed of the actuator.

Hardware improvements include a method to eliminate the switching noise caused by the PWM amplifier. The shielding and filtering reduced the noise to manageable levels, but increased wiring complexity and caused propagation delays in some of the signals. Alternative drive electronics should be investigated to find a solution to this problem.

Appendix A

Actuator Drawings

